CONTENTS Page

Research papers

DOI10.12776/ams.v25i2.1272 p-ISSN 1335-1532
e-ISSN 1338-1156

SYNTHESIS OF $Cu_{1.6}Bi_{4.6}S_8$ COMPOUND FOR THERMOELECTRIC APPLICATION

Binh Ngoc Duong[1)], Long Duc Bui[1)]*
[1)]School of Materials Science and Engineering, Hanoi University of Science and Technology, No. 1, Dai Co Viet Street, Hanoi, Vietnam

Received: 06.11.2018
Accepted: 14.05.2019

[*]Corresponding author: e-mail: binh.duongngoc@hust.edu.vn, Tel: + 842438680355, Department of Non-ferrous Metals and Composites, School of Materials Science and Engineering, Hanoi University of Science and Technology, No. 1, Dai Co Viet, Hanoi, Vietnam

Abstract
In this work, $Cu_{1.6}Bi_{4.6}S_8$ thermoelectric compound was synthesized using high energy milling and heat treatment. The starting mixture include Cu, Bi and S elemental powders at the stoichiometry ratio of the formula $Cu_{1.6}Bi_{4.6}S_8$ were ball milled in a planetary ball mill and heat treated in an electric furnace. The results shown that after 10 hours of milling, a compound identified as $Cu_{3.21}Bi_{4.79}S_9$ was formed. The 16h milled powder was heat-treated at 350, 400 and 450ºC for 1 hours at a heating rate of 8 ºC/minute, XRD of the annealed powder reveals that the $Cu_{3.21}Bi_{4.79}S_9$ obtained fully transformed into $Cu_{1.6}Bi_{4.6}S_8$ after being heat treated at 400ºC. Meanwhile, Bi_2S_3 was found in the powder being annealed at 350ºC. The 5h milled powder was also annealed at 400ºC for 1 hours at a heating rate of 2 and 8 ºC/minute, XRD analysis show that $Cu_{1.6}Bi_{4.6}S_8$ was also formed in the heat-treated powder with the heating rate of 2 ºC/min.

Keywords: bismuth chalcogenide, thermoelectric materials, clean energy material, powder metallurgy

1 Introduction

Energy is central to the survival and prosperity of human society. It is no surprise that sciences consider energy production, consumption and distribution as a major subject of research and development [1, 2]. Currently, the main source of energy in the world is fossil fuels. However, fossil fuel resources are increasingly exhausted along with serious environmental problems arises from their used that have led to the development of new technology to improve the efficiency of fossil fuel usage or finding new energy sources [3-8].

Thermoelectric technology based on thermoelectric materials is an advanced technology for directly converting heat into electricity. When developed to take advantage of waste heat sources, thermoelectric plants help improve energy efficiency and reduce environmental pollution. Thermoelectric equipment has many advantages such as high reliability, has no moving parts and produces no noise and emission [7, 9, 10]. There are different types of thermoelectric materials under development. Each type of thermoelectric material operates efficiently within a specified temperature range: high (>700ºC), medium (~400ºC) and low (<230ºC) [11].

Bi_2Te_3 is one of the most common thermoelectric material for use near room temperatures of up to 230ºC [12-14]. However, Te is considered a toxic and expensive element so research and development are focusing on non-toxic thermoelectric materials such as Bi_2S_3, PbS, CdS, TiS_2 and Ag_2S [15]. At high temperatures, the Si-Ge material is remarkable for its ability to work at temperatures up to 1000°C and is commonly used in spacecraft. However, this material has the

DOI 10.12776/ams.v25i2.1265 p-ISSN 1335-1532
e-ISSN 1338-1156

disadvantage of high thermal conductivity which lowered its conversion coefficient. There have been studies to reduce the thermal conductivity of this type of thermoelectric materials [16-22]. At medium temperature (about 400 ºC), CuS thermoelectric material has many advantages such as: high thermal conversion efficiency, low production cost, low toxicity and abundant supply. This is a common temperature range for the application of thermoelectric materials. As a result, more and more researches are being done to develop thermoelectric materials that operate at medium temperature ranges.

Studies on medium temperature CuS thermoelectric materials began with researches on kesterite (Cu_2ZnSnS_4), digenite ($Cu_{1.8}S$), and chalcopyrite ($CuFeS_2$). Subsequent studies on $Cu_{12-x}Tr_xSb_4S_{13}$ (where Tr is the 3d transition metal and Zn) [23]. Some other materials such as lead telluride, clathrate, silicite, skutterudite also have good conversion efficiency at temperatures of 500-600 °C [2, 24-27].

In this work, $Cu_{1.6}Bi_{4.6}S_8$ thermoelectric compound was synthesized by powder metallurgy. The compound was synthesized from Cu, Bi and S powders, the factors that influence the synthesis process such as milling time and heat treatment condition are also studied.

2 Experimental procedure

In this work, copper (Cu), bismuth (Bi), and sulfur (S) powder were used as the staring materials. The Cu powder was 99.5% of purity (Strem Chemicals Inc.), Bi powder was 99% of purity (Sigma Aldrich), and S powders was 99.5% of purity (Alfa Aesar Co. Ltd). The Cu, Bi and S powder were mixed at an atomic ratio of 1.6:4.6:8 under argon atmosphere.

The powder mixture was then milled using a planetary ball mill (Fritsch Pulverisette 6) with a ball to powder ratio of 10:1 and a milling speed of 300 rpm. The milling process was carried out under argon atmosphere. The obtained milled powder was compacted at 250 MPa using a hydraulic press into a disk shape pellet of 10 mm in diameter and 3 mm in thickness. The compacted pellets were then heat treated in an electric chamber furnace (Nabertherm B150).

Phase analysis was carried out using XRD (Bruker D8 Advance). The surface morphologies and topologies of powder were studied by FE-SEM (Hitachi S-4800). The thermal stability of the milled powder was investigated using a differential scanning calorimeter (Setaram Labsys 18)

3 Results and discussion

3.1 CuBiS compounds prepared under different milling time

Fig. 1 shows the XRD patterns of powders after different milling time. After being milled for 5 h, Cu and S phases were disappeared whereas the intensity of Bi showed little decreased. The results showed that in the incipient stage of milling, the milling energy was not enough to make Bi react with Cu or S, just causing the reaction of Cu and S. The increasing of milling time accumulated energy and Bi powders were gradually involved in the reaction with Cu and S. When the milling time was extended to 10 h, a compound identified as $Cu_{3.21}Bi_{4.79}S_9$ (PDF# 01-073-1202) was detected and the intensity of Bi was vastly reduced. After 16 h of milling, nearly single-phased $Cu_{3.21}Bi_{4.79}S_9$ compound was synthesized.

The formation of $Cu_{3.21}Bi_{4.79}S_9$ was also reported, according to Barma [28], the $Cu_{3.21}Bi_{4.79}S_9$ compound was found after only 5 h of milling whilst the presence of secondary phases such as Bi_2S_3 and Cu_2S were also detected. These secondary phases were disappeared after 15h milling.

This work revealed that the ternary compound $Cu_{1.6}Bi_{4.6}S_8$ cannot be directly synthesized by milling. The final stable compound obtained after the milling process was $Cu_{3.21}Bi_{4.79}S_9$.

DOI 10.12776/ams.v25i2.1265 p-ISSN 1335-1532
e-ISSN 1338-1156

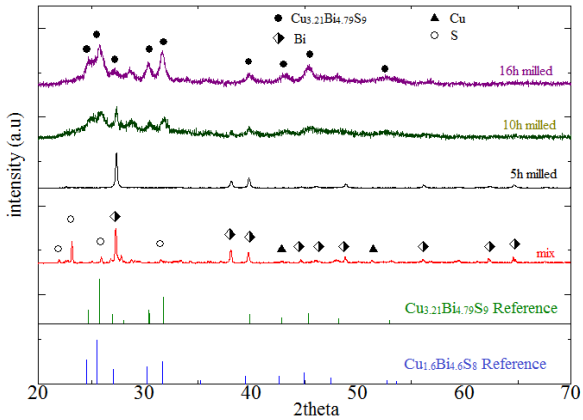

Fig. 1 XRD patterns of the powders after different milling duration

Fig. 2 shows the SEM images of powder obtained at various milling times. After 5 h of milling, the powders were blended together, and the boundary of particles was blurred. The increasing of milling time resulted in finer particles and a homogeneous mixture was obtained after 16 h.

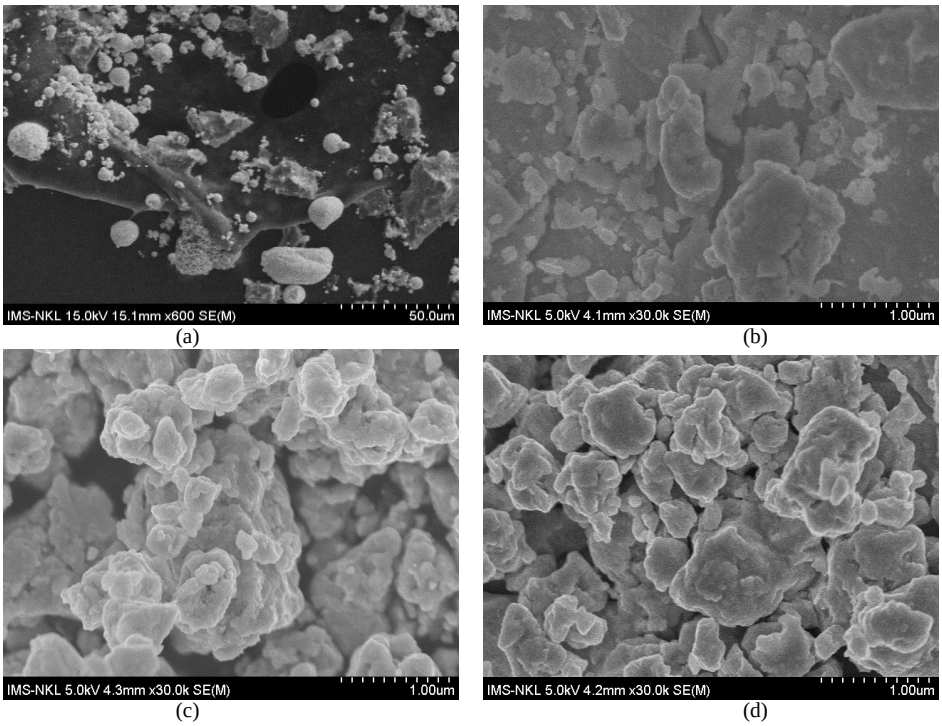

(a) (b)

(c) (d)

Fig. 2 SEM images of powders after a) 0h, b) 5h, c) 10h and d) 16h of milling

3.2 Thermal analysis

The $Cu_{3.21}Bi_{4.79}S_9$ compound obtained after 16 hours of milling was subjected to thermal analysis using a differential scanning calorimeter (DSC) with a heating rate of 8 ºC/min, the DSC curve obtained is shown in **Fig. 3**.

DOI 10.12776/ams.v25i2.1265 p-ISSN 1335-1532
e-ISSN 1338-1156

The DSC curve suggested that there were phases change when the $Cu_{3.21}Bi_{4.79}S_9$ was heated up to 500 ºC. The first phase transformation may have occurred at approx. 280ºC and might be a second change at approx. 430 ºC. The endothermic peak at 280 ºC might have indicated the decomposition of $Cu_{3.21}Bi_{4.79}S_9$ upon heating. Thus, the $Cu_{3.21}Bi_{4.79}S_9$ compound, which also can be used as a thermoelectric material, should not be used for higher than 250 ºC application. In another study [28], the decomposition of $Cu_{3.21}Bi_{4.79}S_9$ was suggested at 260 ºC.

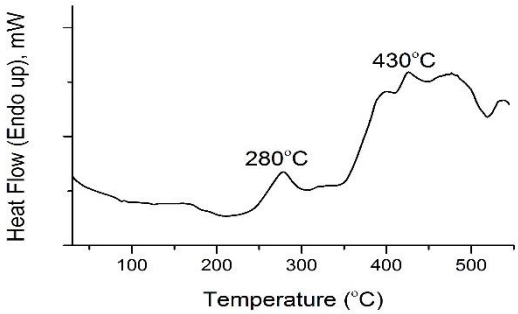

Fig. 3 DSC curve obtained from 16h milled powder

The $Cu_{3.21}Bi_{4.79}S_9$ powder were heat treated at 350, 400 and 450ºC, phase transformation of the compound was investigated using XRD to interpretation of the DSC results. **Fig. 4** shows the XRD patterns of powders at different heat-treated temperature ans the XRD patterns of powders before heat treated. **Fig. 4** has depicted that after being heat treated at 350 ºC, the $Cu_{3.21}Bi_{4.79}S_9$ compound was disappeared in the powder and the present of another compounds, the $Cu_{1.6}Bi_{4.6}S_8$ was detected. It can be concluded that the $Cu_{3.21}Bi_{4.79}S_9$ was transformed into $Cu_{1.6}Bi_{4.6}S_8$, this result confirmed that there was phase changed at 280 ºC as suggested in the DSC curve.

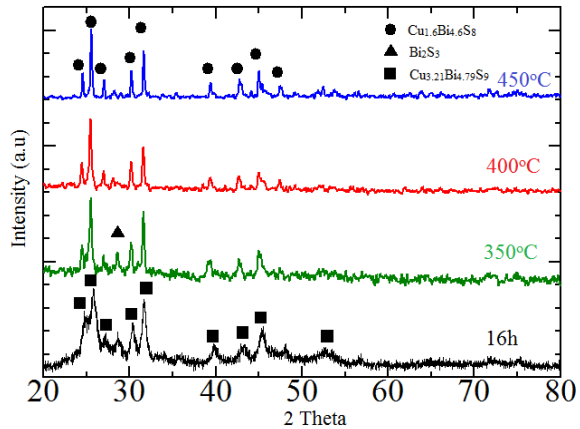

Fig. 4 XRD patterns of powders at different heat-treated temperature

The was also another phased identified in the powder heat tread at 350 ºC, the Bi_2S_3 which was not found in the milled powders. The present of Bi_2S_3 suggested that to some extent, the $Cu_{3.21}Bi_{4.79}S_9$ was not directly transform to $Cu_{1.6}Bi_{4.6}S_8$. The heat treat temperature was not able to convert the $Cu_{3.21}Bi_{4.79}S_9$ powder into $Cu_{1.6}Bi_{4.6}S_8$ powder. At higher heat-treated temperature, the

DOI 10.12776/ams.v25i2.1265 p-ISSN 1335-1532
e-ISSN 1338-1156

Bi_2S_3 peak was no longer appear in the XRD pattern, the obtained powders were solely $Cu_{1.6}Bi_{4.6}S_8$.

3.3 Synthesis of $Cu_{1.6}Bi_{4.6}S_8$ using heat treatment

In order to investigate the effectiveness of the milling process, powder with different milling duration are subjected to similar annealing condition. The compacted powders were heated at the heating rate of 2 ºC/min, the XRD analysis results are shown in **Fig. 5.**

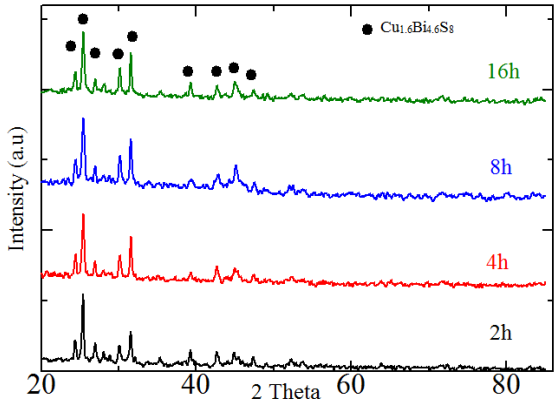

Fig. 5 XRD patterns of powders with different milling duration, heat-treated at 400 ºC

After being heat treated at 400 ºC, $Cu_{1.6}Bi_{4.6}S_8$ was successfully synthesized in all the sample regardless the milling duration. The only phase detected in all cases was $Cu_{1.6}Bi_{4.6}S_8$. The milling process has helped to create a homogeneous powder mixture. It is also provider part of the energy need for the reaction of elemental powders. In this case, it helped in the formation of intermediate phase, the $Cu_{3.21}Bi_{4.79}S_9$, which stabilizer the powder before heat-treating.

The results suggest that it is possible to directly synthesis $Cu_{1.6}Bi_{4.6}S_8$ by heat treatment only. However, the process might require special apparatus and carefully control of the heat-treated conditions such as heating rate and temperature.

4 Conclusion

$Cu_{1.6}Bi_{4.6}S_8$ thermoelectric compound was successfully synthesis using high energy ball milling and heat treatment. The milling process has helped to create a homogeneous powder mixture, provided part of the energy need for the reaction of elemental powders and assist the formation of intermediate phase, the $Cu_{3.21}Bi_{4.79}S_9$, which stabilizer the powder before heat-treating. After 10 hours of milling, $Cu_{3.21}Bi_{4.79}S_9$ was formed and remains the major phase in milled powders. The $Cu_{3.21}Bi_{4.79}S_9$ obtained fully transformed into $Cu_{1.6}Bi_{4.6}S_8$ after being annealed at 400 ºC and above. $Cu_{1.6}Bi_{4.6}S_8$ could also be synthesized form powder with less than 10h of milling. The short-milled powder required carefully control of the heat-treating process.

References

[1] R. Falkner: Energy Research & Social Science, Vol. 1, 2014, p. 188–197, https://doi.org/10.1016/j.erss.2014.03.008

DOI 10.12776/ams.v25i2.1265 p-ISSN 1335-1532
e-ISSN 1338-1156

[2] Fitriani et al.: Renewable and Sustainable Energy Reviews, Vol. 60, 2016, p. 635-659, https://doi.org/10.1016/j.rser.2016.06.035
[3] W. He, G. Zhang, X. Zhang, J. Ji, G. Li, X. Zhao: Applied Energy, Vol. 143, 2015, p. 1-25, https://doi.org/10.1016/j.apenergy.2014.12.075
[4] T. Kvackaj, A. Kovacova, J. Bidulska, R. Bidulsky, R. Kocisko: Archives of Metallurgy and Materials, Vol. 60, 2015, No. 2A, p. 605-614, https://doi.org/ 10.1515/amm-2015-0180
[5] W. Liu, X. Yan, G. Chen, Zh. Ren: Nano Energy, Vol. 1, 2012, Iss. 1, p. 42-56, https://doi.org/10.1016/j.nanoen.2011.10.001
[6] Q. H. Zhang, X. Y. Huang, S. Q. Bai, X. Shi, C. Uher, L. D. Chen: Advanced Engineering Materials, Vol. 18, 2016, No. 2, p. 194-213, https://doi.org/10.1002/adem.201500333
[7] L. E. Bell: Science, Vol. 321, 2008, No. 5895, p. 1457-1461, https://doi.org/10.1126/science.1158899
[8] D. Manfredi, R. Bidulsky: Acta Metallurgica Slovaca, Vol. 23, 2017, No. 3, p. 276-282, https://doi.org/10.12776/ams.v23i3.988
[9] G. J. Snyder, E. S. Toberer: Nature Materials, Vol. 7, 2008, p. 105-114
[10] D. M. Rowe: *CRC Handbook of Thermoelectrics*, 1st edition, CRC Press, 1995
[11] D. Bui, Long, Duong N. Binh, Le M. Hai, Le H. Thang, Tran D. Huy: Vietnam Journal of Science and Technology, Vol. 56, 2018, No. 1A, p. 1-13, https://doi.org/525-2518/56/1A/12498
[12] A. G. Hossam et al.: Annals of Nuclear Energy, Vol. 101, 2017, p. 454–464, https://doi.org/10.1016/j.anucene.2016.12.001
[13] S. LeBlanc: Sustainable Materials and Technologies, Vol. 1-2, 2014, p. 26–35, https://doi.org/10.1016/j.susmat.2014.11.002
[14] D. L. Greenaway, G. Harbeke: Journal of Physics and Chemistry of Solids, Vol. 26, 1965, p. 1585−1604, https://doi.org/10.1016/0022-3697(65)90092-2
[15] Z. H. Ge, L. D. Zhao, D. Wu, X. Liu, B. P. Zhang, J. F. Li, J. He: Materials Today, Vol. 19, 2016, No. 4, p. 227-239, https://doi.org/10.1016/j.mattod.2015.10.004
[16] Y. Kimura, Y. Tamura: Applied Physics Letters, Vol. 92, 2008, (012105), https://doi.org/10.1063/1.2828713
[17] S. R. Culp, J. W. Simonson, S. J Poon, V. Ponnambalam, J. Edwards, T.M. Tritt: Applied Physics Letters, Vol. 93, 2008, (022105), https://doi.org/10.1063/1.2959103
[18] X. Yan, G. Joshi, W. Liu: Nano Letters, Vol. 11, 2011, p. 556–560, https://doi.org/10.1021/nl104138t
[19] H. Muta, T. Kanemitsu, K. Kurosaki, S. Yamanaka: Journal of Alloys and Compounds, Vol. 469, 2009, No. 1-2, p. 50–55, https://doi.org/10.1016/j.jallcom.2008.02.041
[20] S. Populoh et al.: Scripta Materialia, Vol. 66, 2012, Iss. 12, p. 1073–1076, https://doi.org/10.1016/j.scriptamat.2012.03.002
[21] T. Noguchi: Powder processing of thermoelectric materials focusing on SiGe with new sintering technique, Proceedings of 16th International Conference on Thermoelectrics, Germany, 1997, https://doi.org/10.1109/ICT.1997.667082
[22] S. M. Lee, G. C. David: Applied Physics Letter, Vol. 70, 1998, Iss. 22, https://doi.org/10.1063/1.118755
[23] R. S. Jeannine, M.H. Jeremy, J. Song, Journal of Materials Chemistry, Vol. 21, 2011, Iss. 12, p. 4037–4055, https://doi.org/10.1039/C0JM02755C

[24] Z. Houcheng, K. Wei, D. Feifei, X. Haoran, C. Bin, N. Meng: Energy Conversion and Management, Vol.148, 2017, p. 1382–1390, https://doi.org/10.1016/j.enconman.2017.06.089
[25] W. J. Xie et al.: Nano Letters, Vol. 10, 2010, p. 3283-3289, https://doi.org/10.1021/nl100804a
[26] Z. Jiawei, S. Lirong, H. P. Steffen, Y. Hao, T. H. Le, B. I. Bo: Nature Communications, Vol. 8, 2017, (13901)
[27] Z. Huaizhou et al.: Nano Energy, Vol. 7, 2014, p. 97-103, https://doi.org/10.1016/j.nanoen.2014.04.012
[28] M. C. Barma et al.: Powder Technology, Vol. 294, 2016, p. 348–352, https://doi.org/10.1016/j.powtec.2016.03.002

Acknowledgement
This work was supported by Hanoi University of Science and Technology under grant number T2017-PC-067.

EFFECTS OF COOLING RATE ON THE VOLUME FRACTION OF RETAINED AUSTENITE IN FORGINGS FROM HIGH-STRENGTH Mn-Si STEELS

Dagmar Bublíková[1)], Hana Jirková[1)], Kateřina Rubešová[1)], Michal Peković[1)], Julie Volkmannová[1)], Marcel Graf[2)]
[1)] University of West Bohemia, RTI - Regional Technological Institute, Univerzitní 22, CZ – 306 14 Pilsen, Czech Republic
[2)] TU Chemnitz, Professorship Virtual Production Engineering, Straße der Nationen 62, 09111 Chemnitz, Germany

Received: 14.05.2019
Accepted: 04.06.2019

** Corresponding author: e-mail: dagmar.bublikova@seznam.cz, Tel.: +420 720 401 659, Laboratory of Experimental Forming, Faculty of Mechanical Engineering, University of West Bohemia, RTI - Regional Technological Institute, Univerzitní 22, CZ – 306 14 Pilsen, Czech Republic*

Abstract
Various ways are sought today to increase mechanical properties of steels while maintaining their good strength and ductility. Besides effective alloying strategies, one method involves preserving a certain amount of retained austenite in a martensitic matrix. The steel which was chosen as an experimental material for this investigation contained 2.5% manganese, 2.09% silicon and 1.34% chromium, with additions of nickel and molybdenum. An actual closed-die forged part was made of this steel. This forged part was fitted with thermocouples attached to its surface and placed in its interior and then treated using the Qenching and partitioning process. Qenching and partitioning process is characterized by rapid cooling from a soaking temperature to a quenching temperature, which is between the Ms and the Mf, and subsequent reheating to and holding at a partitioning temperature where retained austenite becomes stable. The quenchant was hot water. Cooling took place in a furnace. Heat treatment profiles were constructed from the thermocouple data and the process was then replicated in a thermomechanical simulator. The specimens obtained in this manner were examined using metallographic techniques. The effects of cooling rate on mechanical properties and the amount of retained austenite were assessed. The resultant ultimate strength was around 2100 MPa. Elongation and the amount of retained austenite were 15% and 17%, respectively. Microstructures and mechanical properties of the specimens were then compared to the real-world forged part in order to establish whether physical simulation could be employed for laboratory-based optimization of heat treatment of forgings.

Keywords: closed-die forgings, Q&P process, retained austenite, thermomechanical simulator

1 Introduction

One of the current trends, particularly in the forging industry, is to achieve good mechanical properties and thus long life in products at minimized costs. The available heat treatment methods which can impart high strength and ductility to a material include the Q&P process (Quenching and Partitioning), which leads to strengths in excess of 2000 MPa and elongation levels of about 10% [1-5]. It is characterized by rapid cooling from the austenite region to a temperature between

DOI 10.12776/ams.v25i2.1266 p-ISSN 1335-1532
e-ISSN 1338-1156

the Ms and Mf temperatures, where martensite forms, whereas some austenite remains untransformed. During subsequent isothermal holding, retained austenite (RA) becomes stabilised thanks to carbon which migrates from super-saturated martensite to austenite. According to current knowledge, this retained austenite exists primarily in the form of thin foils between martensite laths or plates [6-8]. To ensure that retained austenite becomes stable, it is important to use the right cooling rate and alloying strategy. They should provide the stability of retained austenite, prevent carbide precipitation within martensite and depress the Ms and Mf [9]. In a majority of advanced high-strength steels, the Ms temperature is in the range of 350°C–400°C. The steel that was used in these experiments was specially designed, with manganese as the dominant alloy addition. In steels of this kind, manganese at higher levels depresses the Ms and Mf temperatures, and therefore enables quenchants other than salt baths to be used. This reduces costs, and is therefore significant to the economy of the process.

2 Experimental material and methods

A special composition was designed for a 0.42 % carbon steel to depress the Ms and Mf, using iterative optimization in the JMatPro program. The Mf was below 100°C, thanks to which boiling water could be used for quenching (Tab. 1). The reduction in Ms and Mf was due mainly to a higher manganese level, i.e. 2.5 % [10]. Other alloying elements included silicon, chromium, and molybdenum [11, 12, 13, 14].

2.1 Data acquisition and development of physical simulation regimes

First, a closed-die forged part was made of the experimental steel (**Fig. 1**). The data for developing physical simula-tion regimes to be conducted in a thermomechanical simulator were gathered in the course of heat treatment of the forged part [15-20]. For this purpose, the part was fitted with thermocouples, some attached to its surface (the fastest-cooling part of the forging) and others placed in its interior (the slowest-cooling location). Specifically, one thermocouple was attached to the surface (no. 1) and two thermocouples were placed in the part's interior (no. 2 and 3), (**Fig. 1**). The forged part was then Q&P processed. It was heated in an air furnace at 880°C to a fully-austenitic condition. Since the special alloying of the steel de-pressed the Mf to 78°C in Table 1, it was possible to use boiling water at 100°C as a quenchant. Boiling water makes a better quenchant than oil or salt baths in terms of safety, the bath quality and degradation, as well as environmental aspects. Once the surface temperature reached approx. 100°C, the part was removed from water and transferred for partitioning for 1 hour in a furnace at 200°C (**Fig. 2**). The thermocouple data from point 1 on the surface indicated that the quenching temperature in that location was 100°C. At points 2 and 3, approx. 10 mm below the surface, the quenching temperature was higher, about 230°C. Several different cooling profiles were thus obtained for several locations across the forged part. The part was then heat-treated again, this time using a different regime. The austenitizing temperature was identical but the cooling step took place in air, until the surface temperature reached 240°C. The purpose was to explore the impact of the cooling rate on the final amount of retained austenite. Austenitizing was followed by partitioning in a furnace at 200°C (**Fig. 3**). In this case, the differences between the measured locations were less distinct than after the water-quenching regime.

Chemnitz Univer-sity of Technology, which collaborated on this investigation, carried out numerical modelling of the heat treatment using FE software Simufact.forming 14.0. Processes with several cooling rates were modelled [6].

DOI 10.12776/ams.v25i2.1266 p-ISSN 1335-1532
e-ISSN 1338-1156

Table 1 Chemical composition of the experimental steel (wt. %)

AHSS	C	Mn	Si	P	S	Cu	Cr	Ni	Al	Mo	Nb	M_s	M_f
	0.419	2.45	2.09	0.005	0.002	0.06	1.34	0.56	0.005	0.04	0.03	209	78

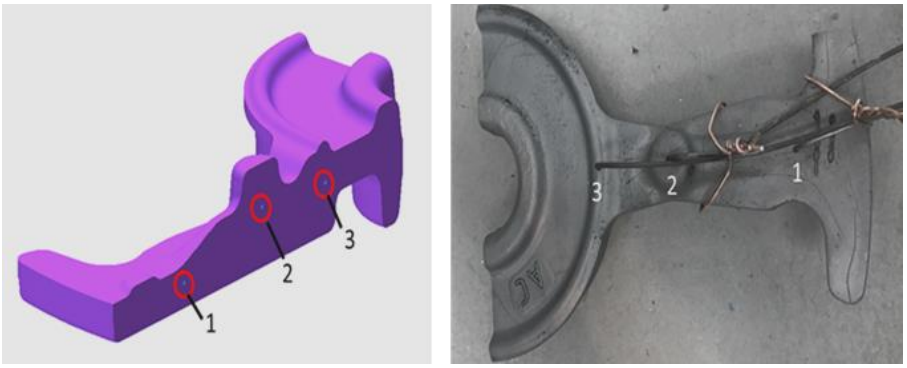

Fig. 1 Closed-die forging of AHSS steel with thermocouples attached for experimental treatment

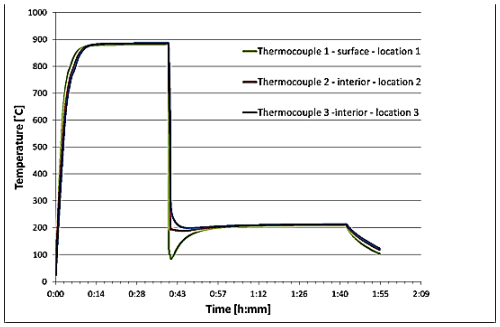

Fig. 2 Q&P processing of the forged part involving quenching in boiling

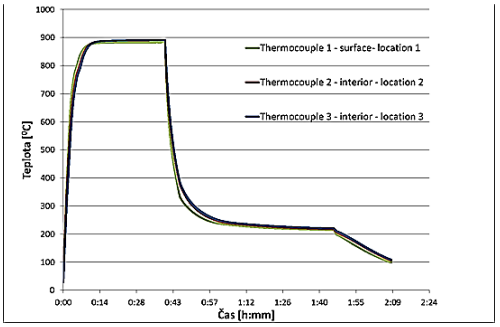

Fig. 3 Q&P processing of the forged part involving cooling in airprocess

3 Physical simulation of cooling of the forged part

Retained austenite in advanced high-strength martensitic steels contributes to their toughness. In order to stabilize retained austenite by Q&P processing, the right quenching temperature must be used along with an appropriate cooling rate. In these experiments, four regimes involving different cooling rates were performed on specimens of the experi-mental steel. The data for designing these regimes were those obtained from heat treatment of the closed-die forged part. The data consisted of cooling curves for quenching in boiling water and for slow cooling in air of the surface and the interior of the forged part (**Fig. 4**).

The first regime was a simulation of quenching of location 1 on the surface of the forged part in boiling water. In this regime, cooling from the soaking temperature to a quenching temperature of approximately 100°C took place at the rate of 64°C/s. It was followed by heating to 200°C and holding for 1 hour. In this time interval, retained austenite in the martensitic matrix became stable. The second regime was a physical simulation of quenching of location 3 within the forged part in boiling water. It comprised cooling at 5.7°C/s to the quenching temperature and the same

DOI 10.12776/ams.v25i2.1266 p-ISSN 1335-1532
e-ISSN 1338-1156

partitioning operation as the previous regime. The third regime was used for simulating air cooling of location 1 on the forged part's surface, using a cooling rate of approx. 3.5°C/s. The subsequent partitioning was performed in a furnace at 200°C for 1 hour. The fourth regime was a physical simulation of air cooling of location 3 in the forged part's interior at a rate of approximately 2.9°C/s (**Fig. 1**). The microstructures and properties of the specimens were then examined and measured using light and scanning electron microscopes and mechanical testing machines, respectively. The amount of retained austenite was determined using X-ray diffraction in **Table 2**.

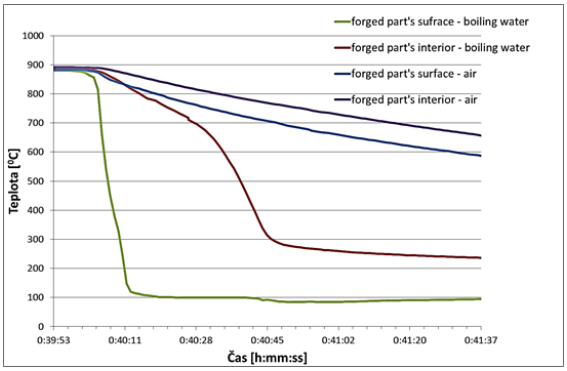

Fig. 4 Detail of cooling curves of the surface and interior of the forged part in the course of quenching in boiling water and cooling in air

Table 2 Heat treatment regimes and mechanical properties

					Physical simulation specimens				Actual forged part			
Regime number	T_A [°C]/t_A [s]	Cooling rate °C/s	QT [°C]	PT [°C/s] /t_{PT} [s]	HV 10 [-]	UTS (R_m) [MPa]	A_{5mm} [%]	Red. of area [%]	HV 10 [-]	UTS (R_m) [MPa]	A_{5mm} [%]	Red. of area [%]
1	880/2400	64	100	200/3600	637	2114	15	17	603	2131	12	10
2		5.7	195	200/3600	669	2250	8	10	643	-	-	9
3		3.5	240	200/3600	692	2009	3	8	666	1949	2	9
4		2.9	240	200/3600	690	2141	4	7	656	2000	1	8

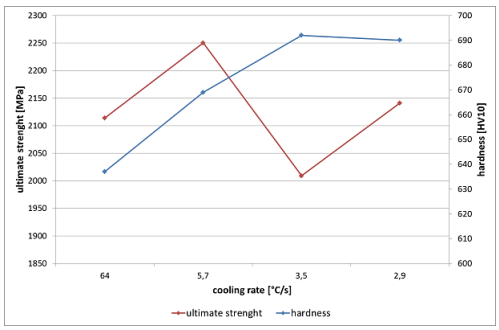

Fig. 5 Dependency ultimate strength and hardness on cooling rate

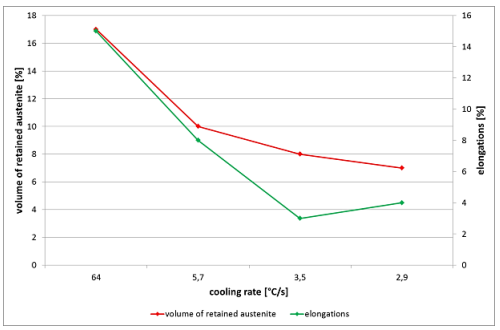

Fig. 6 Dependency alongation and volume of retained austenite on cooling rate

DOI 10.12776/ams.v25i2.1266
p-ISSN 1335-1532
e-ISSN 1338-1156

4 Results and discussion

All the microstructures consisted of a majority of martensite, a small amount of bainite and various volume fractions of retained austenite (**Fig. 7a – 9a**).The volume fraction of retained austenite in the martensitic matrix and other mechanical properties varied with the local cooling rate (**Table 2**, **Fig. 5**, **Fig. 6**). Regime 1 was a simulation of quenching of the surface of the forging in boiling water, and therefore it involved fast cooling (64°C/s). A large volume fraction of retained austenite (17%) in the martensitic matrix of this specimen was found by X-ray diffraction analysis. It was confirmed by light microscopic observation of special two-stage-etched metallographic sections (1st etching step: nital, 2nd step: 10% aqueous solution of $Na_2S_2O_5$) (**Fig. 7b**). Retained austenite was present as globular grains and as particles between martensite needles. Regime 2 involved slower cooling, at 5.7°C/s. It was a simulation of the forged part's interior during quenching in boiling water. After this regime, the ultimate strength was about 100 MPa higher than in the previous case. As the amount of martensite was larger than in the previous case, hardness and elongation was higher (**Table 2**, **Fig. 5**). Most of it was in the form of globular grains. Some was found between martensitic needles. Two subsequent regimes were similar to each other. They were simulations of air cooling of the surface and interior of the forged part. Their cooling rates were low: 3.5°C/s and 2.9°C/s, respectively. As a consequence, the resulting elongations were even lower than in the previous case (**Table 2**, **Fig. 6**). A small amount of retained austenite was in a globular form (**Fig. 8b**). Mechanical properties of the specimens more or less corresponded to those of the real forged part (**Table 2**). The largest amount of retained austenite, 10%, was found in the surface of the forged part upon quenching in boiling water. Retained austenite was present as globular grains and as particles between martensite needles (**Fig. 9b**). The ultimate strength of the forged part, 2131 MPa, and its elongation of 12% are nearly identical to those of the physical simulation specimens in **Table 2**.

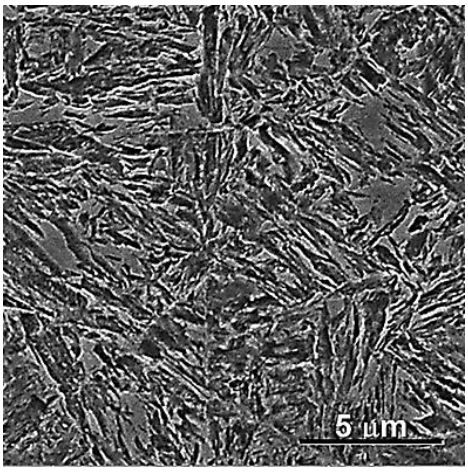

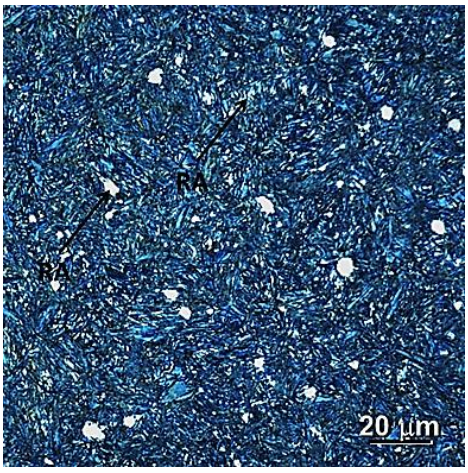

Fig. 7 a) Physical simulation of cooling of the forged part's surface, cooling rate: 64°C/s, martensitic structure, bainite, retained austenite, detail scanning electron micrograph

b) Physical simulation of cooling of the forged part's surface, cooling rate: 64 °C/s, colour etching to reveal retained austenite, optical micrograph

DOI 10.12776/ams.v25i2.1266 p-ISSN 1335-1532
e-ISSN 1338-1156

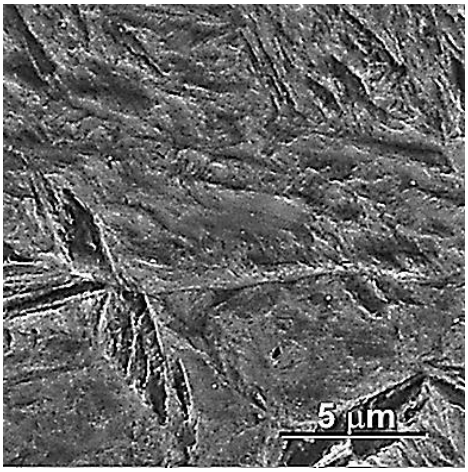

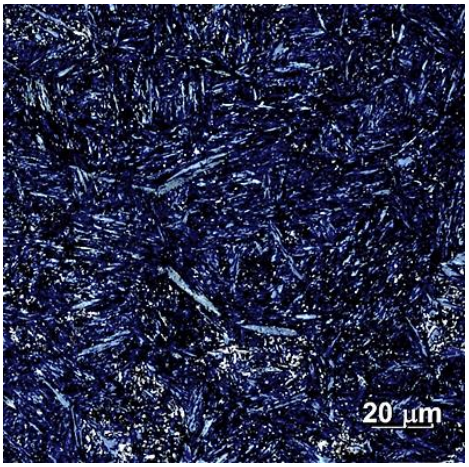

Fig. 8 a) Physical simulation of cooling of the forged part's surface, air, cooling rate: 3.5 °C/s, martensitic structure, a small amount of bainite, retained austenite, detail scanning electron micrograph

b) Physical simulation of cooling of the forged part's interior, cooling rate: 3.5 °C/s, colour etching to reveal retained austenite, optical micrograph

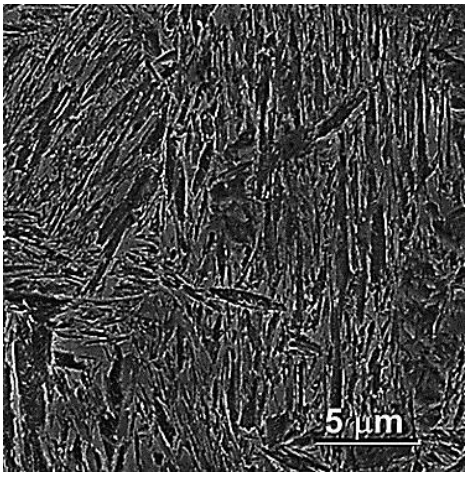

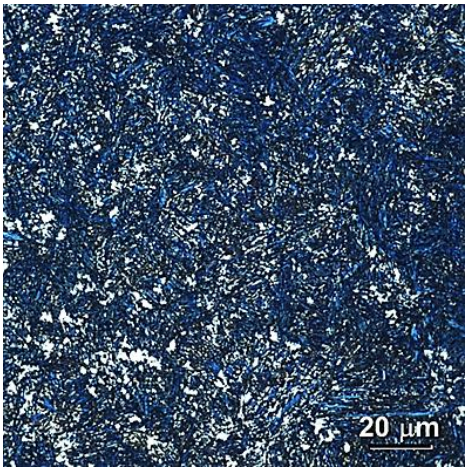

Fig. 9 a) The actual forged part, cooling rate: 64 °C/s, boiling water, martensitic structure, bainite, retained austenite, detail scanning electron micrograph

b) The actual forged part, cooling rate: 64 °C/s, martensit-ic structure, bainite, retained austenite, colour etching to reveal retained austenite, optical micrograph

5 Conclusion

Physical simulation regimes with various cooling profiles (64°C/s, 5.7°C/s, 3.5°C/s and 2.9°C/s) demonstrated the substantial impact that cooling rates have on the resulting amount of retained austenite in martensitic matrix. Upon cooling at the highest rate, which corresponded to quenching of the forged part's surface in hot water, some austenite failed to decompose into martensite. As

DOI 10.12776/ams.v25i2.1266 p-ISSN 1335-1532
e-ISSN 1338-1156

a result, a considerable volume fraction of austenite remained present as a stable phase in the martensitic matrix, thanks to appropriate alloying. The regime, which involved this particular cooling rate, led to a high elongation, as high as 15%, and an ultimate strength of approximately 2100 MPa. Regimes with slow cooling, which physically simulated cooling of the interior of the forged part in hot water and in air, provided smaller amounts of retained austenite in martensitic matrix, sometimes as low as 8%. Higher hardness levels, which were caused by larger volume fractions of martensite, were associated with markedly lower elongations. Mechanical properties of the AHS steel after physical simulation of treatment of the forged part were in agreement with the values for the actual forged part. Fast cooling (64°C/s) in boiling water led to a strength of 2130 MPa and elongation of 12%.

The comparison between physical simulation and the real-world forged part suggests that physical simulation in the laboratory enables a wide range of heat treatment parameters to be tested for optimizing the processing of closed-die forgings.

References

[1] D. V. Edmondsa, K. Hea, F. C. Rizzo, B. C. De Coomanc, D. K. Matlock: Quenching and partitioning martensite - A novel steel heat treatment, Materials Science and Engineering A, 2006, Vol. 438–440, p. 25–34, https://doi.org/10.1016/j.jallcom.2012.02.016

[2] B. Mašek, H. Jirková, D. Hauserová, L. Kučerová, D. Klaubeová: The Efe Effect of Mn and Si on the Properties of Advanced High Strength Steels Processed by Quenching and Partitioning, Materials Science Forum, Vol. 654-656, 2010, p. 94-97, https://doi.org/10.4028/www.scientific.net/MSF.654-656.94

[3] H. Jirková, L. Kučerová, B. Mašek: Effect of Quenching and Partitioning Temperatures in the Q-P Process on the Properties of AHSS with Various Amounts of Manganese and Silicon, Materials Science Forum, Vol. 706-709, 2012, p. 2734-2739, https://doi.org/10.4028/www.scientific.net/MSF.706-709.2734

[4] T. Y. Hsu (XuZuyao), X. J. Jin, Y. H. Rong: Strengthening and toughening mechanisms of quenching–partitioning–tempering (Q–P–T) steels, Journal of Alloys and Compounds, Vol. 577, 2013, p. S568–S571, https://doi.org/10.1016/j.jallcom.2012.02.016

[5] J. G. at al.: The Quenching and partitioning process: Background and Recent Progress. Materials Reasearch. 2005, Vol. 8, No. 4, p. 417-423

[6] H. Jirková, et al.: Influence of metastable retained austenite on macro and micromechanical properties of steel processed by the Q-P process, Journal of Alloys and Compounds, available online, Journal of Alloys and Compounds, 2014, Vol. 615, p. 163–168, https://doi.org/10.1016/j.jallcom.2013.12.028

[7] Z. Qian, Q. Lihe, T. Jun, M. Jiangying, Z. Fucheng: Inconsistent effects of mechanical stability of retained austenite on ductility and toughness of transformation-induced plasticity steels, Materials Science & Engineering A, 2013, Vol. 578, p. 370–376, doi.org/10.1016/j.msea.2013.04.096

[8] E. De Moor, D. Matlock, at al.: Austenite stabilization through manganese enrichment, Scripta Materialia, January 2011, Vol. 64, p. 185–188, https://doi.org/10.1016/j.scriptamat.2010.09.040

[9] K. Ibrahim, D. Bublíková, H. Jirková, B. Mašek: Stabilization of Retained Austenite in High-Strength Martensitic Steels with Reduced Ms Temperature, In METAL 2015, Ostrava: TANGER spol. s r. o., 2015, p. 1-7, ISBN: 978-80-87294-58-1

[10] H. Jirková, L. Kučerová, B. Mašek: Effect of Quenching and Partitioning Temperatures in the Q-P Process on the Properties of AHSS with Various Amounts of Manganese and Silicon, Materials Science Forum, Vol. 706-709, 2012, p. 2734-2739, https://doi.org/10.4028/www.scientific.net / MSF.706-709.2734
[11] E. V. Pereloma, I. B. Timokina, P. D. Hodgson: Transformation behavior in thermomechanical processed C-Mn-Si steel with and without Nb, Materials Science and Engineering A 273-275,1999, p. 448-452
[12] W. Bleck: Using the TRIP efekt – the down of a promising group of cod formable steelos, Proccedings of International Conference on TRIP – Aided High Strenght Ferrous Alloys, 2002, Belgium
[13] S. Baik, S. Kim, S. Jin, O. Kwon: Effect of alloying elements on mechanical propeties and phase transformation of cold rolled TRIP steel steels, ISIJ International, 2001, Vol. 41, No. 3, pp. 290-297
[14] S. H. Park, W. Y Choo, N. J. Kim, J. H. Ko: Effects of hot rolling conditions on the microstructure and tensile properties of Nb-bearing TRIP steels, International Symposium on Hot Workability and Light Alloys Composites, TMS of CIM, Motrioll Quebek, 1996, Canada, p. 493
[15] M. Graf, S. Härtel, A. Bauer, W. Förster, D. Bublíková, M. Wagner, B. Awiszus, B. Mašek: Development of a Quenching-Partitioning Process Chain for Forging Components, Materials Science Forum, 2018, Vol. 918, p. 89-92, https://doi.org/10.4028/www.scientific.net/MSF.918.85
[16] V. Pileček, F. Vančura, H. Jirková, B. Mašek: Material-Technological Modelling of the Die Forging of 42CrMoS4 Steel, Materials and Technology, Vol. 48, 2014, p. 869-873
[17] I. Vorel, F. Vančura, B. Mašek: Material - Technological Modelling of Controlled Cooling of Closed die Forgings from Finish Forging Temperature. In METAL 2015 24th International Conference on Metallurgy and Materials, Ostrava: 2015 TANGER Ltd., 2015, p. 202-208, ISBN: 978-80-87294-62-8
[18] Š. Jeníček, I. Vorel, J. Káňa, K. Opatová: The Use of Material-Technological Modelling to Determine the Effect of Temperature and Amount of Deformation on Microstructure Evolution in a Closed-Die Forging Treated by Controlled Cooling, Manufacturing Technology, Vol. 17, 2017, p. 326-330
[19] J. Káňa, I. Vorel, A. Ronešová: Simulator of Thermomechanical Treatment of Metals, In Daaam 2015. Vienna: Daaam International Vienna, 2016, p. 0513-05018, ISBN: 978-3-902734-07-5, ISSN: 1726-9679
[20] B. Mašek, H. Jirková, J. Malina, L. Skálová, L. W. Meyer: Physical Modelling of Microstructure Development During Technological Processes with Intensive Incremental Deformation, Key Engineering Materials, Vol. 345-346, 2007, p. 934-946, https://doi.org/10.4028/www.scientific.net / KEM.345-346.943

Acknowledgements

The present contribution has been prepared under project LO1502 'Development of the Regional Technological Institute' under the auspices of the National Sustainability Programme I of the Ministry of Education of the Czech Republic aimed to support research, experimental development and innovation.

USE OF MULTI-PHASE TRIP STEEL FOR PRESS-HARDENING TECHNOLOGY

Hana Jirková[1)], Kateřina Opatová[1)], Štěpán Jeníček[1)], Jiří Vrtáček[1)], Ludmila Kučerová[1)], Petr Kurka[2)]*
[1)] University of West Bohemia, RTI-Regional Technological Institute, Pilsen, Czech Republic
[2)] Anchor Lamina GmbH, Chemnitz, Germany

Received: 14.05.2019
Accepted: 16.06.2019

[*]Corresponding author: e-mail: hstankov@rti.zcu.cz, Tel.: +420 377 63 8782, Regional Technological Institute, University of West Bohemia, Univerzitní 22, 30100 Pilsen, Czech Republic

Abstract
Development of high strength or even ultra-high strength steels is mainly driven by the automotive industry which strives to reduce the weight of individual parts, fuel consumption, and CO_2 emissions. Another important factor is to improve passenger safety. In order to achieve the required mechanical properties, it is necessary to use suitable heat treatment in addition to an appropriate alloying strategy. The main problem of these types of treatments is the isothermal holding step. For TRIP steels, the holding temperature lies in the field of bainitic transformation. These isothermal holds are economically demanding to perform in industrial conditions. Therefore new treatments without isothermal holds, which are possible to integrate directly into the production process, are searched. One way to produce high-strength sheet is the press-hardening technology. Physical simulation based on data from a real-world press-hardening process was tested on CMnSi TRIP steel. Mixed martensitic-bainitic structures with ferrite and retained austenite (RA) were obtained, having tensile strengths in excess of 1000 MPa.

Keywords: High Strength Steel, Press-hardening, TRIP steel, heat treatment

1 Introduction

Advanced high-strength steels (AHSS) are a promising group of materials for the automotive industry. Since most of them are multiphase materials that benefit from a number of strengthening mechanisms, considerably wide ranges of mechanical properties can be attained [1-3]. They enable the car body weight and fuel consumption to be reduced while improving crash safety [4, 5]. Thanks to their properties they are used for safety components in car bodies [6, 7].
TRIP (TRansformation Induced Plasticity) steels, which possess a good combination of strength and ductility, fall into this group [8, 9]. Their microstructures consist of ferrite, carbide-free bainite and retained austenite (RA) [8-15]. Upon cold deformation, RA transforms into high-carbon martensite which substantially contributes to work hardening [9, 14]. Work hardening is further enhanced by dislocations and internal stresses within the surrounding phases [10].
One of the processes, by which such high-strength components can be manufactured, is press hardening. The process enables sheet stock of hardenable materials to be worked using comparatively low forming forces and leads to a reduced springback [16-18]. The difficulty with TRIP steels is the requirement for isothermal holding which is technologically complicated to meet [16]. If the multiphase microstructure and therefore the desired mechanical properties are to be obtained, various cooling regimes in press hardening need to be tested.

DOI 10.12776/ams.v25i2.1267 p-ISSN 1335-1532
e-ISSN 1338-1156

2 Experiments

For this experiment, several press hardening-based variants of heat treatment were proposed. The data for developing the regimes were measured in real-world press hardening processes. The regimes simulated normal press hardening in a tool at different temperatures and broken quenching with different cooling rates.

2.1 Experimental material

The CMnSi TRIP is a low-alloy 0.2% carbon steel alloyed with Mn and Si (**Table 1**). This composition was chosen for the sake of stability of RA, for solid solution strengthening, and to prevent carbide precipitation during bainite formation [9, 10]. Specimens for heat treatment were made from a soft-annealed sheet 1.5 mm in thickness. Its structure consisted of ferrite and pearlite; its hardness was 190 HV10 (**Fig. 1**). The ultimate strength reached 627 MPa and elongation A_{20} was 26%. Phase transformations were identified by calculation performed with the JMatPro software (Release 9.0, 2016).

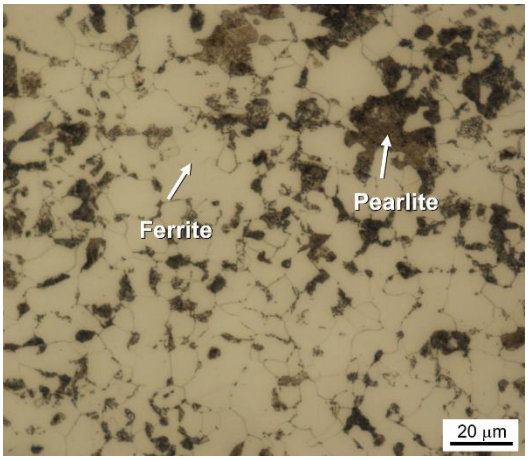

Fig. 1 Initial structure of TRIP steel

Table 1 The chemical composition of the experimental steel [wt. %]

C	Mn	Si	Al	Nb	P	S	Ni	M_s [°C]	M_f [°C]
0.21	1.4	1.8	0.006	0.002	0.007	0.005	0.07	363	249

2.2 Physical simulation of press hardening with different cooling parameters

Instead of conducting trials of new materials or processes in a production plant, which would hamper commercial operation, laboratory physical simulations can be performed using a thermomechanical simulator which offers fast heating and cooling (up to 200°C/s). The data for developing the present simulation regimes were measured in a real-world process, with the tool either at RT or pre-heated to various temperatures.

In the first regime, the tool was at room temperature (RT) (**Fig. 2a**). The first step was soaking at 937°C for 100 seconds. The subsequent step (idle time), which took 7 seconds, was a simulation of the workpiece cooling in the air during transfer from the furnace to the forming tool. The temperature dropped to 760°C. Simulation of press hardening in a tool at RT followed, where the

DOI 10.12776/ams.v25i2.1267 p-ISSN 1335-1532
e-ISSN 1338-1156

cooling rate was 100 °C/s (**Table 2**). In the other regimes of this kind, the simulation of press hardening was based on tool temperatures of 300–600°C and was followed by air cooling (**Table 2, Fig. 2a**).

Table 2 Influence of the tool temperature on the mechanical properties

Heating temp. [°C]	Tool temp. [°C]	$R_{p0.2}$ [MPa]	R_m [MPa]	A_{20} [%]	HV10 [-]	RA [%]
937	Room temp. (RT)	900±15	1340±13	7±3	471±3	3
	300	857±4	1130±15	6±3	407±8	7
	425	568±10	977±5	15±3	323±3	10
	600	440±16	903±17	16±3	277±4	-

Table 3 Mechanical properties after broken quenching

Heating temp. [°C]	Cooling rate above 425°C [°C/s]	Cooling rate below 425°C [°C/s]	$R_{p0.2}$ [MPa]	R_m [MPa]	A_{20} [%]	HV10 [-]
937	16	1	482±16	925±17	15±3	285±2
	16	0.5	471±8	882±5	17±2	280±1
	10	1	436±12	898±11	18±2	279±3

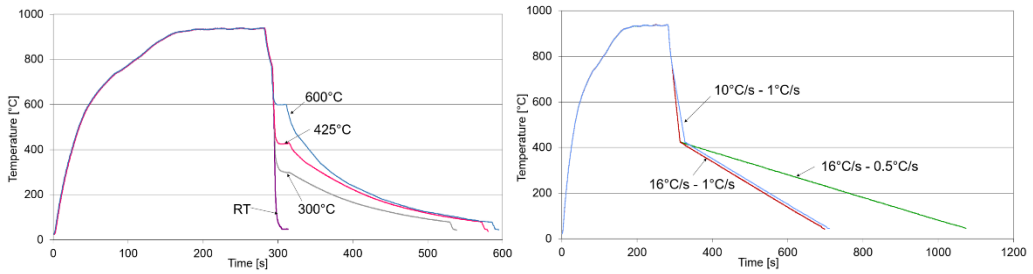

Fig. 2 Examples of regimes for physical simulation of press hardening: a) tool with different temperatures, b) broken quenching

In another group of regimes, the effect of broken quenching was explored, where the slower-cooling stage began at 425°C (**Fig. 2b**). This temperature was chosen on the basis of earlier experiments and findings from intercritical annealing of this steel [19, 20]. The rates of cooling from 760°C, i.e. after the idle time, were either 16°C/s or 10°C/s, being applied down to 425°C. According to the calculation with JMatPro, these cooling rates will guarantee that ferrite forms in the material. The cooling curves, at the same time, do not intersect the pearlite nose in the diagram. Slower cooling from 425°C to RT, at 1°C/s or 0.5°C/s, was expected to support bainite formation – without holding at 425°C (**Table 3**).

Microstructures were examined using optical (OM) and scanning electron microscopy (SEM). The amount of RA was measured using X-ray diffraction on the automatic powder diffractometer AXS Bruker D8 Discover.

3 Results and discussion

The regime, which was a physical simulation of press hardening in a tool at RT, where the cooling rate was 100°C, produced a martensitic microstructure with some ferrite and 3% RA (**Fig. 3a**).

DOI 10.12776/ams.v25i2.1267 p-ISSN 1335-1532
e-ISSN 1338-1156

This structure did not represent the typical TRIP structure, because the formation of bainite was not supported by holding time at the temperature above M_s and the cooling rate in the area was too fast for bainite development. The hardness value was 471 HV10. The ultimate strength was 1340 MPa and elongation reached 7% (**Table 2**). The formation of ferrite-martensite structure in the TRIP steel after treatment without holding time was also described by J. Tian et. al. [21]. Besides, K. Sugimoto tried to develop TRIP steels with a martensitic annealed matrix with improved formability for auto-auto body manufactures [15, 22]. The possibility of processing by press-hardening for high strength steels with direct quenching was also presented by Mori et al. [4]. In the next regime, higher tool temperature was simulated, 300°C, which promoted the formation of proeutectoid ferrite. This led to lower ultimate strengths, 1130 MPa, but no significant changes in elongation. The regime with a simulated tool temperature of 425°C produced a microstructure with a majority of bainite blocks, some free ferrite and a small volume fraction of martensite (**Fig. 3b**). The amount of RA was 10%. The formation of bainite was supported by a slower cooling rate after cooling to 425°C and almost typical structure for TRIP steels was obtained. Elongation was higher than in previous regimes, 15%, whereas strength was lower, 977 MPa. The regime, which simulated cooling in a tool at 600°C, led to a mixture of ferrite and martensite and a low volume fraction of bainite (**Fig. 3c**). In addition, a small amount of pearlite was found along grain boundaries. The ultimate strength was lower than in the previous case, 903 MPa, accompanied by elongation 16%.

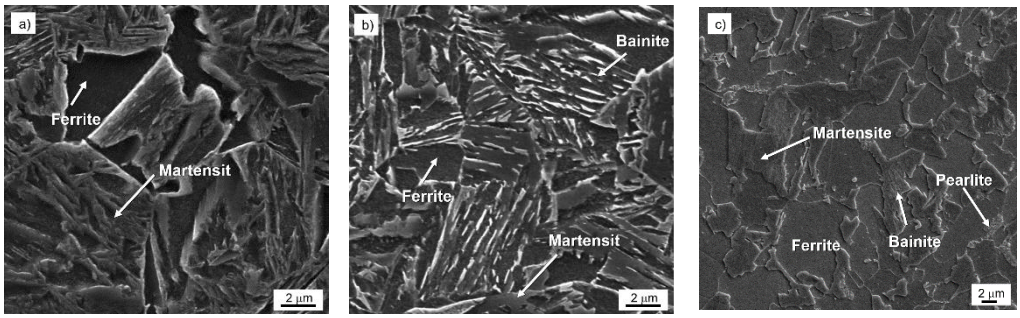

Fig. 3 Microstructural evolution in relation to tool temperature: a) RT, b) 425°C, c) 600°C

The simulated broken quenching regime with cooling rates above and below 425°C of 16°C/s and 1°C/s, respectively, led to a mixture of ferrite, bainite, martensite and RA (**Table 3, Fig. 4a**). Since the rate of cooling above 425°C was slower than in the corresponding press hardening regime, free ferrite was obtained. Very slow cooling rate below 425°C made it possible for bainite to form. The transformation to bainite was incomplete. The remaining unstable austenite then decomposed into martensite once the M_s had been reached. Upon this regime, the ultimate strength was 925 MPa, combined with elongation of 15% (**Table 3**). The regime, in which cooling below 425°C was even slower (0.5°C/s), promoted bainite formation (**Fig. 4b**). In the regime, in which the first stage of cooling was slower than in the previous regimes, i.e. 10°C/s instead of 16°C/s, the transformation to pearlite was slightly more effective along prior austenite grain boundaries. The resulting fraction of bainite was thus lower (**Fig. 4c, Table 3**). The formation of perlite from the cooling rate 10°C/s in the area of perlitic transformation was also confirmed by A. Pichler et al. [23]. They described the influence of cooling rate on the kinetic of bainitic transformation, ferrite growth and the amount of retained austenite.

DOI 10.12776/ams.v25i2.1267 p-ISSN 1335-1532
e-ISSN 1338-1156

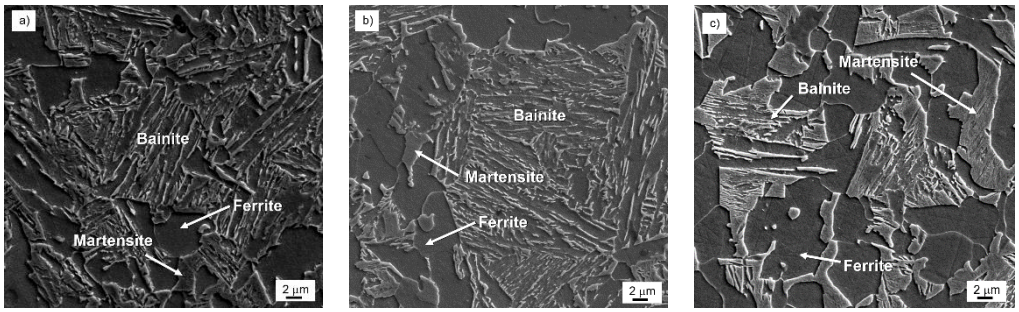

Fig. 4 Microstructures upon different cooling profiles: a) 16°C/s – 1°C/s, b) 16°C/s – 0.5°C/s, c) 10°C/s – 1°C/s

4 Conclusion

Press hardening with different cooling parameters was physically simulated on low-alloy TRIP steel. The simulated press hardening with a tool at RT produced a martensitic structure with a small amount of ferrite. Its ultimate strength and elongation were 1340 MPa and 7%, respectively. The regime in which the simulated tool temperature was higher, 425°C, led to free ferrite and bainite and stabilized RA. It had a favourable impact on elongation: 15%, accompanied by strength of 977 MPa. The broken quenching regimes with much slower cooling below 425°C, led to the intensive formation of bainite and ferrite. Their strengths were 925–882 MPa with elongations of 15–17%.

References

[1] E. Girault, et al.: Scripta Materialia, Vol. 44, 2001, p. 885-892, https://doi.org/10.1016/S1359-6462(00)00697-7

[2] J. Zhao, Z. Jiang: Progress in Materials Science, Vol. 94, 2018, p. 174–242, https://doi.org/10.1016/j.pmatsci.2018.01.00

[3] H. Aydin, E. Essadiqi, I. Jung, S. Yue: Materials Science and Engineering A, Vol. 564, 2013, p. 501–508, https://doi.org/10.1016/ j.msea.2012.11.113

[4] K. Mori, et al.: CIRP Annals - Manufacturing Technology, Vol. 66, 2017, No. 2, p. 755–777, https://doi.org/10.1016/j.cirp.2017.05.007

[5] [10.12.2018], https://automotive.arcelormittal.com/News/2329/S-in_motionMid-sizeGDIS2016

[6] P. Christodoulou: Effect of retained austenite transformation on the fatigue behavior of aluminum containing TRIP steels, Ph.D. thesis, University of Thessaly, Volos, Greece, 09/2017

[7] [10.12. 2018], https://automotive.arcelormittal.com/europe/products/ AHSS/TRIP/EN

[8] I. B. Timokhina, P. D. Hodgson, E. V. Pereloma: Metallurgical and Materials Transactions A, Vol. 35A, 2004, p. 2331–2341, https://doi.org/10.1007/s11661-006-0213-9

[9] W. Bleck: Using the TRIP effect - the dawn of a promising group of cold formable steels, In.: International Conference on TRIP-Aided High Strength Ferrous Alloys, Ghent, Mainz/Aachen, GRIPS, Bad Harzburg p. 13–23, 2002

[10] S. Ch. Baik, S. Kim, Y. S. Jin, O. Kwon: ISIJ International, Vol. 41, 2001, No. 3, p. 290-297, https://doi.org/10.2355/isijinternational.41.290

[11] L. Kučerová, H. Jirková, A. Jandová: Acta Metallurgica Slovaca, Vol. 23, 2017, No. 3, p. 244-250, https://doi.org/10.12776/ams.v23i3.968

[12] W. Bleck, W. Guo, M. Yan: Steel Research International, 2017, Vol. 88, 2017, No. 10, p. 1-21, https://doi.org/10.1002/srin.201700218
[13] J. Chiang, J. D. Boyd, K. Pilkey, K. Keith: Materials Science and Engineering A, Vol. 638, 2015, p. 132–142, https://doi.org/10.1016/j.msea.2015.03.069
[14] B. C. De Cooman: Current Opinion in Solid State and Materials Science, Vol. 8, 2004, No. 3-4, p. 285–303, https://doi.org/10.1016/j.cossms.2004.10.002
[15] K. Sugimoto, M. Mukherjee: TRIP aided and complex phase steels. In.: Automotive Steel, edited by R. Rana, S. B. Singh, Woodhead Publishing - Elsevier, United Kingdom, 2017, p. 217–257, https://doi.org/10.1016/B978-0-08-100638-2.00008-0
[16] H. Karbasian, E. A. Tekkaya: Journal of Materials Processing Technology, Vol. 210, 2010, No. 15, p. 2103–2118, https://doi.org/10.1016/j.jmatprotec.2010.07.019
[17] R. Neugebauer, et al.: Archives of Civil and Mechanical Engineering, Vol. 12, 2012, No. 2, p. 113-118, https://doi.org/10.1016/j.acme.2012.04.013
[18] H. Järvinen, M. Isakov, T. Nyyssönen, M. Järvenpää, P. Peura, Materials Science and Engineering: A, Vol. 676, 2016, p. 109-120, https://doi.org/10.1016/j.msea.2016.08.096
[19] H. Jirková, K. Opatová, J. Káňa, M. Bystrianský: Manufacturing Technology, Vol. 18, 2018, No. 2, p. 243-247, https://doi.org/10.21062/ujep/85.2018/a/1213-2489/MT/18/2/243
[20] L. Kučerová, H. Jirková, B. Mašek: Materials Today: Proceedings, Vol. 2, 2015, No. 3, p. S677-S680, https://doi.org/10.1016/j.matpr.2015.07.374
[21] Y. Tian et al.: C , Mn Partitioning Behavior of Low Carbon Si-Mn Steel in I&Q Process, In.: ICAS 2016 & HMnS 2016, Chengdu, China, p. 521–524, 2016
[22] K. Sugimoto, A. Kanda, R. Kikuchi, S. Hashimoto, T. Kashima, S. Ikeda: ISIJ International, Vol. 42, 2002, No. 8, p. 910-915, https://doi.org/10.2355/isijinternational.42.910
[23] A. Pichler, S. Traint, M. Blaimschein, J. Sperl, P. Stiaszny, E. A. Werner: Correlation between thermal treatment, retained austenite stability and mechanical properties of low-alloyed TRIP steels. In.: International Conference on TRIP-Aided High Strength Ferrous Alloys, Ghent, Mainz/Aachen, GRIPS, Bad Harzburg, 2002, p. 171–180, 2002

Acknowledgement

This paper was prepared under project no. LO1502 "Development of the Regional Technological Institute" under the auspices of the National Sustainability Programme I of the Ministry of Education of the Czech Republic.

EFFECT OF TiO_2 NANOPARTICLES ON THE MECHANICAL AND ANTICORROSIVE PROPERTIES OF Zn-Ni COMPOSITE COATINGS

Nadjette Belhamra[1)], Abd Raouf Boulebtina[1)], Okba Belahssen[1)]*
[1)] Physic Laboratory of Thin Films and Applications (LPCMA), University of Biskra, 07000, Algeria

Received: 14.05.2019
Accepted: 16.06.2019

**Corresponding author: bel_okba@yahoo.fr, Tel: +21374637626, Physic Laboratory of Thin Films and Applications (LPCMA), University of Biskra, 07000, Algeria*

Abstract
In this paper, we are interested in the study of electrochemical, morphological and structural characteristics of the properties of the deposits of Zn-Ni-TiO_2 obtained by electrodeposition on the mild steel substrate in a bath of sulfate. The principal aim is to improve the coatings with better properties, by incorporation of titanium oxide, which is a hard compound, chemically stable and irreducible. The characterization of the coatings was carried out by scanning electron microscopy (SEM) and by X-ray diffraction. The morphology of the film surface varies with the concentration of oxide titanium and it was found higher values of microhardness. Electrochemical characterization of the composites had been carried out through potentiodynamic polarization. The results showed that better corrosion resistance with the incorporation of oxide titanium.

Keywords: Zn-Ni coating, titanium oxide, electrodeposition, morphology, corrosion

1 Introduction

The materials, like humans, need to be well protected from external attack. The main aggressive agents are wear and corrosion. So we took the habit of removing them from this risk by deposits of hard layers and / or protective. The use of coatings for mechanical piece has become widespread, in particular to improve their lifetime.

The elaboration of these coatings involves numerous and varied techniques which make it possible to obtain the wide range of coatings, each having very specific qualities and characteristics. Electrodeposition is one of the most technologically realizable and economically superior techniques for the production of metal matrix composites.

The use of zinc and zinc alloys to improve the corrosion resistance of coated steel sheets has been widely studied due to its importance in industrial contexts. Zn-Ni, Zn-Co and Zn-Fe alloys being the most widely used [1-3].

Zn-Ni alloy is widely used for the corrosion protection of steel, especially in the automotive industry [4]. However, these alloys have low hardness and abrasion resistance with content of nickel, which could be improved by ceramic particle incorporation.

The most important nanoparticles used as deposits are oxides or carbides such as Al_2O_3 [5-7], TiO_2 [8- 11], SiO_2 [12, 13], ZrO_2 [7], SiC [7].

TiO_2 has been used to improve different metallic and organic coatings. TiO_2 with a metallic coating significantly contributes to wear and corrosion resistance, better [8-10, 12]. Vlasa et al. [13] indicated that the porous nanocomposite coatings exhibit higher corrosion resistance when compared to pure Zn coatings and is strongly affected by the TiO_2 structure and concentration.

DOI 10.12776/ams.v25i2.1268 p-ISSN 1335-1532
e-ISSN 1338-1156

The zinc metal matrix with TiO_2 nanoparticles predominantly shows higher corrosion resistance property due to considerable morphological changes in the deposit and it is confirmed by our previous report on the corrosion behavior of zinc-TiO_2 nanocomposite.
In this context, Zn-Ni-TiO_2 composite coating on steel was prepared by electrodeposition process. The electrolyte is aqueous solution containing zinc and nickel salts with uniformly dispersed TiO_2 nanoparticles. The study also examines the corrosion resistance property of composite with reference to alloy coating.

2 Experimental methodologies

2.1 Coating preparation

Zn-Ni and Zn-Ni-TiO_2 coatings were deposited on mild steel substrates using sulfate bath. The constituents of the bath are illustrated in **Table 1**. The cathode was the mild steel plane and anode was pure zinc (99.99%). The mild steel planes were polished mechanically, degreased in an alkaline solution and treated with HCl (10%). The electrodeposition process was carried out time approximately 30 min under the conditions: T = 30 °C, pH = 3 and density current was J = 3 $A.dm^{-2}$.
The composite deposits were prepared by addition of TiO_2 in the electrolyte in a range from 0 to 20 g. L^{-1} and a pitch of 5 g. L^{-1}. The nanoparticles are added and stirred for 48 hours to assure good dispersion. The pH of the solution is controlled by the addition of the aqueous HCl or NaOH solutions.

Table 1 Electrolyte compositions [14]

Composition	Concentration [$g.L^{-1}$]
Zinc sulfate ($ZnSO_4$, $7H_2O$)	57.5
Nickel sulfate ($NiSO_4$, $6H_2O$)	52.5
Sodium sulfate (Na_2SO_4)	56.8
Sodium citrate ($Na_3C_6H5O_7$, $2H_2O$)	56.8
Boric acid (H_3BO_3)	9.3

2.2 Coating characterization

After the realization of coatings, they are placed in a thermal furnace at 200 °C for 30 minutes to control their adhesion; this method is called thermal shock. It is evident that this object is achieved only if the coating is well adhered to the substrate, the adhesion therefore authorize the quality of the preparation of the surface to be coated and the quality of the coating operation.
The surface morphology of the coatings was examined using a Quanta TM 250 scanning electron microscope (SEM). X-ray diffraction characterization of samples was carried out with a D8 Advance-Brucker uses a Cu Kα line at λ = 0.1540 nm in the 2θ ranged from 10° – 95° in steps of 0.02 ° at a scan speed 2 °/min.
Microhardness of the Zn–Ni coatings was measured using Vickers hardness Zwick Roell with 100 g load for 10 seconds.
The corrosion tests were carried out in a neutral aqueous NaCl (35 $g.L^{-1}$) solution, naturally aerated. The test device was composed of a PGZ301 potentiostat and a 1L cell containing electrolytes, into which three electrodes were plunged: the calomel reference electrode saturated in KCl (SCE), the platinum counter electrode and the specimen as the working electrode. In order to determine the corrosion behavior of a specimen immersed in the electrolyte, the curves I (E) are plotted from ± 200 mV versus the corrosion potential using a sweep rate of 10 mV. min^{-1}.

DOI 10.12776/ams.v25i2.1268 p-ISSN 1335-1532
e-ISSN 1338-1156

3 Results and discussions

3.1 Structure and morphology of coating obtained

3.1.1 X-ray diffraction

The analyze of x-ray diffraction patterns of the coatings obtained shows the existence of different phases such as: α-phase (Zn) at the preferred orientations (100), (110), (112) and (201). All the detectable peaks could be indexed to hexagonal structure as that are found in the standard reference data (JCPDS No. 00-001-1238), and γ- phase (Ni5Zn21) at orientations (321), (330) (521). All the detectable peaks could be indexed to cubic structure as that are found in the standard reference data (JCPDS No. 00-006-0653). This result is according to the recent researches [15-16]. In the presence of TiO_2 corresponding to the tetragonal structure which is consistent with the JCPDS No. 98-000-19161, the intensity of the few peaks changes, this indicates the change in their crystalline size **(Fig.1)**. The peak (330) is the most intense orientation for the Zn-Ni coating.

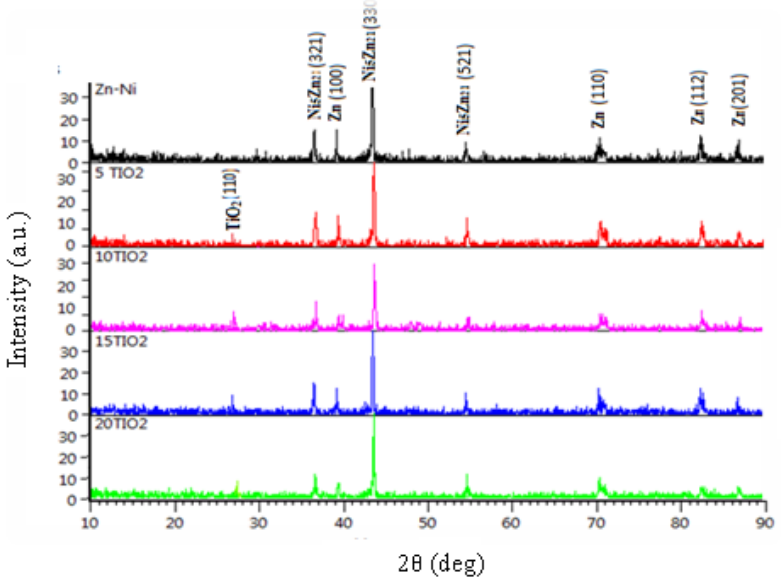

Fig. 1 XRD patterns of Zn–Ni alloy coatings electrodeposited at different concentrations of TiO_2

The grain size of the coatings was determined from X-ray peak broadening by applying the Scherer formula (1) which is well suited to detect a grain size of less than 100 nm [17-18]:

$$D = \frac{0{,}9\lambda}{\beta cos\theta} \quad (1)$$

where D is the grain size, is the X-ray wavelength (λ = 1.5406 Å), β is the full width at half-maximum (FWHM), and θ is Bragg angle position of peak.

For the most intensive peak (330), the grain size for the Zn-Ni and Zn-Ni-15 $g.L^{-1}$ TiO_2 coatings is 0.84 nm, 0.63 nm for the two Zn-Ni-5 $g.L^{-1}$ and 10 $g.L^{-1}$ of TiO_2 and 0.5 for the Zn-Ni-20 $g.L^{-1}$ TiO_2 coating respectively, this indicate that the composite coatings have a size smaller than the grain alloy coatings, the incorporation of TiO_2 nanoparticles in the coating has refined crystals. It should be noted that all the particle sizes of the coatings are in nanometric scale, it confirmed the nanocrystalline structure of the composite coatings Zn-Ni and Zn-Ni-TiO_2.

DOI 10.12776/ams.v25i2.1268 p-ISSN 1335-1532
e-ISSN 1338-1156

3.1.2 Surface morphology

The SEM images show the changes in morphological and structural of the deposits with the addition of the TiO_2 in the bath. We also observed the presence of TiO_2 in the form of small white dots that are distributed throughout the deposit **Fig. 2**.

It can be clearly seen that the size of the crystals has been reduced by the incorporation of TiO_2 from the results of DRX, the small peak at $2\theta = 27.43°$ corresponds to TiO_2. It gives evidence of the presence of TiO_2 in the coating. The thickness of the coating is 80 μm.

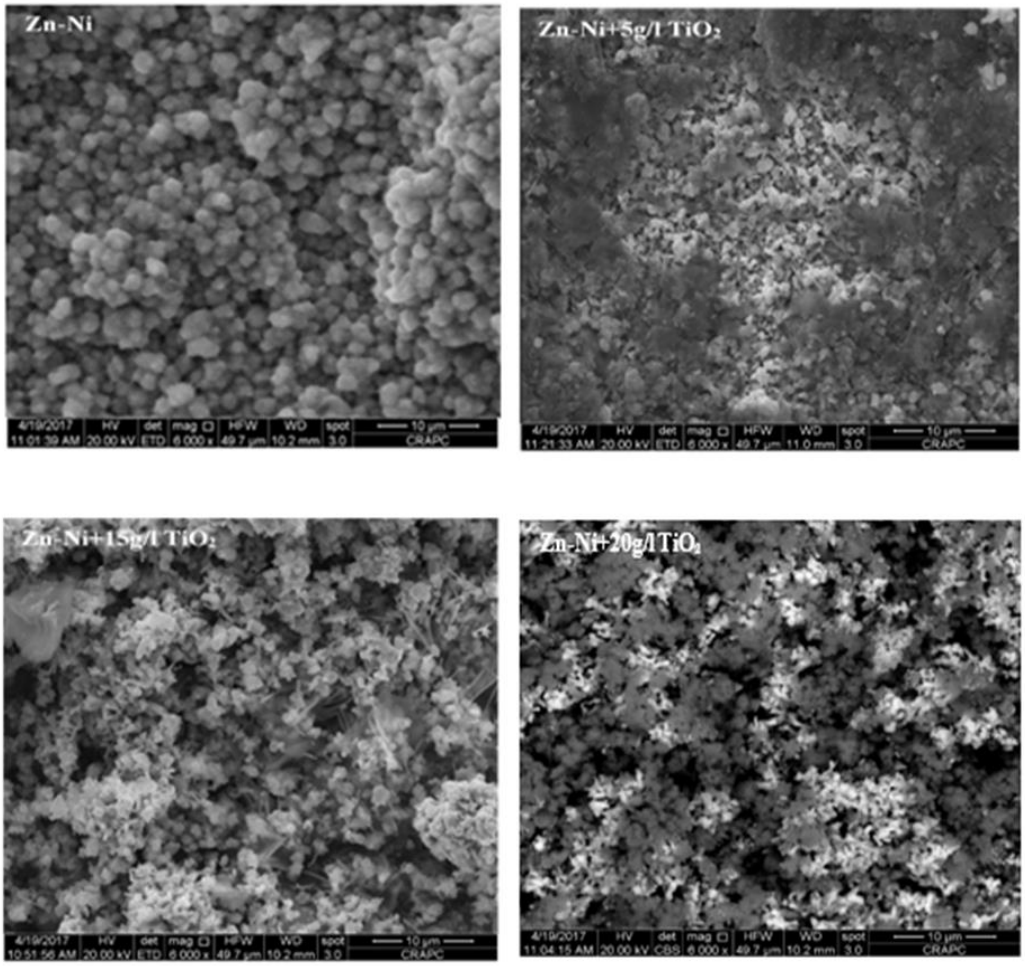

Fig. 2 SEM image of Zn-Ni deposits with different concentrations of TiO_2

3.2 Microhardness of Zn-Ni-TiO2 coatings

The compositional variables in microhardness of Zn-Ni alloys have been investigated by various researchers [18-22]. Zn-Ni alloys are harder than pure Zn. In our studies, the microhardness of the coatings increased with the addition of TiO_2 nanoparticles. This increase is due essentially to the heterogeneity of the coating, and consequently improves the mechanical properties of the deposits. The results obtained are given in **Table 2.**

DOI 10.12776/ams.v25i2.1268 p-ISSN 1335-1532
e-ISSN 1338-1156

Table 2 Values of micro-hardness (HV)

Concentration of TiO_2 ($g.L^{-1}$)	Micro-hardness (Hv)
0	106
5	120
10	123
15	144
20	178

3.3 Corrosion behavior studies of the coatings

The corrosion test of different coating Zn-Ni-TiO_2 with the potentiodynamic polarization curves are displayed in **Fig. 3**. The cathodic and anodic tafel slopes βc and βa respectively and the corrosion current densities (I_{corr}) are obtained graphically by the intersection of the anodic and cathodic tafel lines extrapolated to the corrosion potential (E_{corr}), estimating that the kinetic of electrochemical reactions responsible for corrosion is limited by the charge transfer step, the values of the electrochemical parameters determined from previous polarization curves obtained are presented in **Table 3**.

Table 3 The electrochemical parameters (E_{corr}, I_{corr}, βa, βc, R_p, τ_{corr}) of the coatings samples in 3.5 % NaCl solution

Concentration of TiO_2 ($g.L^{-1}$)	E_{corr} (mV)	I_{corr} ($mA.cm^{-2}$)	β_a (mV/dec)	β_c (mV/dec)	R_p ($\Omega.cm^2$)	τ_{corr} ($mm.y^{-1}$)
0	-1358.20	2.69	85.0	-160.3	14.52	31.55
5	-1082.70	0.54	305.2	-198.2	75.38	6.36
10	-1151.10	0.22	143.0	-157.2	206.75	2.64
15	-1096.10	0.01	77.1	-148.9	3830.00	0.13
20	-1263.40	0.26	2812.1	-90.6	118.81	3.04

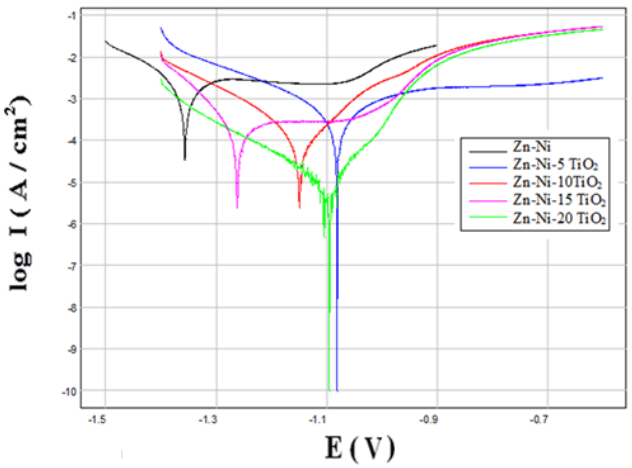

Fig. 3 Polarizing curves obtained for the alloy coatings in a 3.5 % NaCl solution at different concentrations of TiO_2

The analysis of the parameters obtained by the interpretation of the polarization curves revealed less negative Ecorr values (**Fig. 3**), a smaller Icorr value and a larger polarization resistance (Rp)

DOI 10.12776/ams.v25i2.1268 p-ISSN 1335-1532
e-ISSN 1338-1156

value for the nanocomposite coatings. These results indicate that Zn-Ni-TiO_2 composite coatings are resistant to corrosion. We can observe that the optimal concentration of TiO_2 nanoparticles in the electrolytic is 15 g. L-1. We can say that the incorporation of TiO_2 in the coating reducing the corrosion rate (τcorr). An explanation has been given by Saied et al. [9], in which they mentioned that TiO_2 nanoparticles changes the structure of the metal deposition, which is most fine, because the nanoparticles provide more nucleation sites and delay the growth of Zn-Ni matrix. TiO_2 nanoparticles also fill defects and improve corrosion resistance and hardness.

4 Conclusion

The objective of this work was to investigate the effect of TiO_2 on the properties of Zn-Ni composite coatings which was deposited on mild steel substrates by electrodeposition from a sulfate bath. From the results, the following conclusions can be drawn:

- X-ray patterns of all the coatings show only the presence of cubic γ-phase Ni_5Zn_{21}.
- The size of the crystals was reduced by the incorporation of TiO_2, the small peak at 27.43 (2θ) corresponds to TiO_2, indicating that these particles refined the crystals.
- Vickers microhardness measurements showed that the incorporation of TiO_2 leads to an increase in hardness.
- The optimal concentration of TiO_2 nanoparticles in the electrolyte is 15 $g.L^{-1}$; it gives the best corrosion resistance.

References

[1] G. Barceló, J. García, M. Sarret, C. Müller, J. Pregonas, Properties of Zn-Ni alloy deposits from ammonium baths. Journal of Applied Electrochemistry, Vol. 24, 1994, No.12, p. 1249-1255, https://doi.org/10.1007/BF00249889

[2] E. Gómez, X. Alcobe, E. Vallés, Characterisation of zinc+cobalt alloy phases obtained by electrodeposition. Journal of Electroanalytical Chemistry, Vol. 505, 2001, No. 1–2, p. 54-61, , https://doi.org/10.1016/S0022-0728(01)00450-8

[3] C.Q. Yang, Y.C. Zhou, Z.L. Long, Electrodeposition and physico-chemical properties of Zn-Fe alloy coatings from sulfate solution. J Mater Sci Lett Vol. 21, 2002, No. 21, p. 1677-1680, https://doi.org/10.1023/A%3A1020876726469

[4] H.Y. Zheng, M. An and J.Lu, Surface characterization of the Zn–Ni–Al2O3 nanocomposite coating fabricated under ultrasound condition, J. Appl. Surf. Sci., C.Q. Yang, Y.C. Zhou, Z.L. Long, Electrodeposition and physico-chemical properties of Zn-Fe alloy coatings from sulfate solution. J Mater Sci Lett Vol. 254, 2008, p. 1644, https://doi.org/10.1016/j.apsusc.2007.07.110

[5] A. Seza, H. Jafarian, M. Hasheminiasari, M. Aliofkhazraei, Effect of Duty Cycle on Corrosion Resistance and Mechanical Properties of Tertiary Al2O3/ Y2O3/Graphene Pulsed Electrodeposited Ni-Based Nano-Composite. Procedia Materials Science Vol. 11, 2015, p. 576 – 582, https://doi.org/10.1016/j.mspro.2015.11.077

[6] Y. M. Han and M. Farzaneh, Synthesis and characterization of CeO2-Al2O3 nanocomposite coating on the AA6061 alloy, Advanced Materials Research, Vol. 1120-1121, 2015, p. 750-762, https://doi.org/10.4028/www.scientific.net/AMR.1120-1121.750

[7] G. Roventi, G. Giuliani, M. Pisani, T. Bellezze, Electrodeposition of Zn-Ni-ZrO2, Zn-Ni-Al2O3 and Zn-Ni-SiC Nanocomposite Coatings from an Alkaline Bath. Int. J. Electrochem. Sci., Vol.12, 2017, p. 663 – 678, https://doi.org/10.20964/2017.01.40

[8] O.S.I. Fayomi and A. P. I. Popoola, Anti-corrosion Properties and Structural Characteristics of Fabricated Ternary Coatings. J.Surface Engineering and Applied Electrochemistry, Vol. 51, 2015, No.1, p.76–84, https://doi.org/10.3103/S1068375515010068
[9] S. Saied, A. Mekkaoui, O. Belahssen, A. Chala, Effect of TiO2 nanoparticles in Ni matrix on mechanical and corrosion resistance properties, Acta Metallurgica Slovaca, Vol. 23, 2017, No.1, p. 37-44, https://doi.org/10.12776/ams.v23i1.846
[10] U. Yathish, A. Chitharanjan Hegde, Corrosion protection of electrodeposited multilayer nanocomposite Zn-Ni-SiO2 coatings, J. Surface Engineering and Applied Electrochemistry, Vol. 49, 2013, No. 2, p. 164–167, https://doi.org/10.3103/S1068375513020142
[11] O. Hammami, L. Dhouibi, P. Bercot, E.M. Rezrazi and E. Triki, Study of Zn-Ni Alloy Coatings Modified by Nano-SiO2 Particles Incorporation, Int. J. Corros. , Vol. 2012, 2012, https://doi.org/10.1155/2012/301392
[12] P.M. Praveen, T.V. Venkatesha, Y.A. Naik, K. Prashantha, Corrosion behavior of Zn- TiO2 composite coating, Synthesis and Reactivity in Inorganic, Metal-Organic and Nano- Metal Chemistry. Vol. 37, 2007, No. 6 p. 461-465, https://doi.org/10.1080/15533170701471216
[13] A. Vlasa, S. Varsara, A. Pop, C. Bulea, and L. M. Muresan, Electrodeposited Zn–TiO2 nanocomposite coatings and their corrosion behavior, J. Appl. Electrochem., Vol. 40, 2010, p. 1519-1527, https://doi.org/10.1007/s10800-010-0130-x
[14] M. Diafi, N. Belhamra, H. Ben Temam, B. Gasmi, S. Benramache, Effect of ni doping on some properties of electrodeposited zinc alloy coatings, Acta Mettalucgica Slovaca, Vol. 21, 2015, No 3, p. 226-235, https://doi.org/10.12776/ams.v21i3.472
[15] M. Mortaga Abou-Krisha, Electrochemical studies of zinc–nickel codeposition in sulphate bath Applied Surface Science. Vol. 252, 2005, No.4, p. 1035-1048, https://doi.org/10.1016/j.apsusc.2005.01.161
[16] A. Petrauskas, L. Grincevicienne, L. Cesuniné, R. Juskenas, Studies of phase composition of Zn–Ni alloy obtained in acetate-chloride electrolyte by using XRD and potentiodynamic stripping, Electrochimica Acta. Vol. 50, 2005, No. 5, p. 1189-1196, https://doi.org/10.1016/j.electacta.2004.07.044
[17] M.M. Abou-Kirsha, F. Elkhatabi, M. Sarret, C. Müller, Dependence of coating characteristics on deposition potential for electrodeposited Zn–Ni alloys, Electrochimica Acta. Vol. 44, 1999, No. 10, p. 1645-1653 https://doi.org/10.1016/S0013-4686(98)00286-2
[18] O. Belahssen, M. Ghougali, A. Chala. Effect of Iron Doping on Physical Properties of NiO Thin Films. Journal of Nano- and Electronic Physics , Vol.10, 2018, No.2, 02039(4pp), https://doi.org/10.21272/jnep.10(2).02039
[19] G. Barceló, E. García, M. Sarret , C. Müller, J. Pregonas, Characterization of zinc–nickel alloys obtained from an industrial chloride bath, Journal of Applied Electrochemistry, Vol. 28, 1998,No 10, p.1113-1120, https://doi.org/10.1023/A:1003461109203
[20] L. Felloni, R. Fratesi, E. Quadrini, G. Roventi, Electrodeposition of zinc-nickel alloys from chloride solution. Journal of Applied Electrochemistry, Vol. 17, 1987, No.3, p.574-82 https://doi.org/10.1007/BF01084132
[21] A.M. Alfantazi, U. Erb, Microhardness and thermal stability of pulse-plated Zn-Ni alloy coatings. Materials Science and Engineering: A, Vol. 212, 1996, p.123-129, https://doi.org/10.1016/0921-5093(96)10187-8
[22] I. Books, U. Erb, Hardness of electrodeposited microcrystalline and nanocrystalline gamma-phase Zn-Ni alloys, Scripta Mater. Vol. 44, 2001, No. 5, p.853-858, https://doi.org/10.1016/S1359-6462(00)00680-1

STRUCTURE OF HIGH-CARBON STEEL AFTER WELDING WITH RAPID COOLING

Yurii Kalinin[1)], Michail Brykov[2)], Ivan Petryshynets[3)], Vasily Efremenko[4)], Olaf Hesse[5)], Maik Kunert[5)], Michail Andrushchenko[2)], Michail Osipov[2)], Stanislav Berezhnyy[2)], Oleg Bykovskiy[2)]*
[1)] *PJSC Zaporozhtransformator, Zaporizhzhia, Ukraine*
[2)] *Zaporizhia National Technical University, Zaporizhzhia, Ukraine*
[3)] *Institute of Materials Research Slovak Academy of Sciences, Košice, Slovakia*
[4)] *Pryazovskyi State Technical University, Mariupol, Ukraine*
[5)] *Ernst-Abbe-Hochschule Jena, Jena, Germany*

Received: 14.05.2019
Accepted: 16.06.2019

* *Corresponding author:* brykov@zntu.edu.ua, *Tel: +38 061 7698262, Welding Department, Zaporizhzhia National Technical University, Zhukovsky 64, 69063 Zaporizhzhia, Ukraine*

Abstract
In this paper the effect of rapid cooling during arc welding on the structure of fusion layer and heat affected zone (HAZ) of high-carbon low alloyed steel have been studied. The main idea was that despite of high carbon content (1.2%) it is necessary to achieve quenching in HAZ. Due to proper chemical composition of welded steel martensite start temperature Ms is about 20 °C, therefore austenitic structure of quenched metal is preserved after rapid cooling. Exposition of HAZ to excessive heat during welding cycle leads to local precipitation of carbides from austenite and thus raising of Ms. In this case some amount of martensite was present in structure after cooling along with austenite and carbides. Microstructure, microhardness and chemical composition of remelted electrode metal, fusion zone and HAZ were studied by means of optical microscopy, SEM, EDX and microhardness testing.

Keywords: wear resistance, high-carbon low-alloyed steels, welding, rapid cooling, austenite, martensite

1 Introduction

Wear is addressed to as one of major problems in modern industry. Any machine part that works in moving contact under load with some counter body always suffer from wear, which is gradual loss of material from contact surface. Ultimate wear may vary from several tenths of micrometers, for example in elements of diesel engine fuel pumps [1] or dies for assembling car body parts [2-4] to tenth of millimeters for parts of blast furnaces [5] or milling and crushing equipment in mineral processing industries working under abrasive wear [6].

Reducing wear loss may be achieved in several ways. Widely used methods are deposition of protective layers by surfacing [7-9], optimization of bulk heat treatment [10, 11, 12] or surface modifying treatment [13-16] of properly chosen wear resistant compositions. Recently new class of wear resistant materials for abrasive wear environment is proposed. That is high-carbon low-alloyed steels [17-19]. Due to high carbon concentration (1.2%) and about 3% of alloying elements it is possible to reduce martensite start temperature Ms as low as to 10-30 °C when quenching from single-phase γ-domain. Therefore the amount of retained austenite after quenching these steels in water at room temperature achieves 90-100% [19]. Because of high

DOI 10.12776/ams.v25i2.1269 p-ISSN 1335-1532
e-ISSN 1338-1156

sensitivity of that austenite to phase transformation under mechanical impact – for example scratching during abrasive wear – thin hard layer (up to 11 GPa depending on abrasive conditions) of mechanically induced martensite is instantly forming on worn surface enabling higher abrasive wear resistance of steel [19].

High carbon content is beneficial for wear resistance of steel but simultaneously worsens its weldability. Steels with carbon equivalent 0.4 and higher are considered to have poor weldability [20, 21]. It is well-adopted that the higher carbon or other alloying elements (except Co) are present in austenite the less is a cooling rate needed to avoid formation of martensitic structure [22]. Therefore the more carbon and other elements are contained in steel (carbon equivalent) the more probable is appearing of martensite in heat affected zone (HAZ) after welding which leads to cracks in HAZ (i.e. steel poor weldability). Preheating these steels before welding leads to decreasing cooling rate in HAZ below critical level hence martensite formation can be suppressed. Post-welding heat treatment provides decomposition of martensite if any appears within HAZ during welding thermal cycle.

Steels with carbon content above 0.5-0.8 wt.% are not widely used in welding joints. Ms temperature for carbon concentrations 0.5-0.8 wt.% is high enough, therefore the retained austenite in HAZ is not considered as a factor influencing mechanical properties. If for some reasons Ms is decreased to room temperature or lower, then martensite would not be present in HAZ at all, and all efforts aimed to avoid martensite formation (pre-heating and post-welding heat treatment) would not be necessary. This is the case for welding high-carbon (about 1.2 wt.%) low-alloyed (about 3 wt.% of alloying elements in total) steels which possess 100 vol.% of retained austenite after quenching due to Ms to be at about of 20 ^{o}C. Regarding these steels preheating and post-welding thermal treatment would negatively affect the structure of retained unstable austenite, thus abrasive wear resistance of welded parts would be dramatically decreased. Therefore rapid cooling in HAZ is vitally needed to provide fully austenitic structure avoiding pearlite formation in the vicinity of fusion line. This will allow obtaining welding joints with higher wear resistance.

Currently rapid cooling is used at most as technique to improve mechanical properties of HAZ formed during friction stir welding of Al-based alloys [23, 24], Fe-based alloys with different carbon content [25, 26, 27]. Some techniques like explosion welding or laser welding involve rapid cooling without any special efforts [28, 29], although even during laser welding especially accelerated cooling is sometimes necessary [30]. Concluding, rapid cooling is a known technique used in welding however intended rapid cooling in HAZ during welding of high-carbon low-alloyed steels is not studied and substantiated yet.

Basing on above considerations, the object of present work was studying the model weld joint of high-carbon low-alloyed steel focusing on microstructure formed in HAZ under rapid cooling.

2 Experimental materials and methods

Industrially manufactured 5mm thick and 60 mm wide strip of steel 120Mn3Si2 was used for welding experiment. Chemical composition of steel was as follows: 1.21 wt% C, 2.56 wt% Mn, 1.59 wt % Si. Rectangular workpiece of this strip was quenched from 1000 ^{o}C into water to obtain fully austenitic structure.

Welding with rapid cooling was imitated by fast single touch of electrode with the edge of workpiece. The touch initiated arc spark with current of 130 A at a voltage of 25 V. The reverse polarity was used to increase heat input. As a result single welding "joint" shown in **Fig.1** was formed from base material and remelted electrode metal. The heat generated by the arc was

DOI 10.12776/ams.v25i2.1269 p-ISSN 1335-1532
e-ISSN 1338-1156

quickly dissipated through heat conductivity into workpiece. The temperature of HAZ was controlled by chromel-copel thermocouple that was welded to the flat side of workpiece in a distance of 5 mm from its edge. The "Time-Temperature" correlation corresponding to welding cycle is presented in **Fig. 2**.

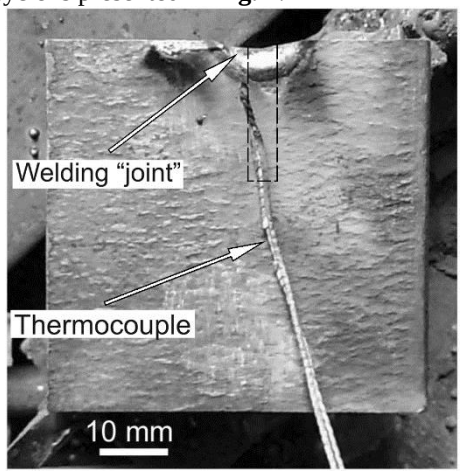

Fig. 1 Experimental workpiece with single welding "spot"

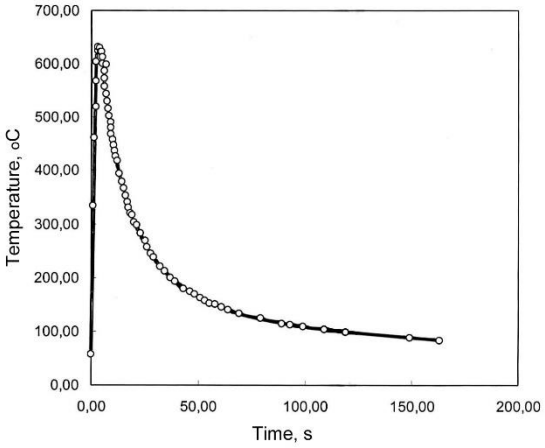

Fig. 2 "Time-Temperature" correlation corresponding to welding cycle

According to **Fig. 2** thermocouple junction have been almost contacted with liquid metal. Nevertheless the peak temperature was much lover than melting point of steel and even Ac_1. This may be explained by very short welding cycle (less than 1 s) and fast cooling due to heat conductivity into cold base metal. As a result, the heat input to thermocouple junction appeared to be insufficient to increase temperature to higher values than that recorded.

The sample of about 20 mm long and about 5 mm wide was cut from the workpiece as shown in **Fig. 1** by dashed line. Sample's cross-section was polished and etched with 4 vol% nital. Microstructure of HAZ was investigated by means of SEM (JEOL JSM-7000F) and optical microscopy (OLYMPUS GX-71). Local EDX analysis was performed using SEM (TESCAN) equipped with Bruker EDX detector. Microhardness was measured by computer controlled Wilson® Hardness tester.

3 Results and discussion

Panorama compiled by low magnification optical micrographs depicting microstructure of welding "joint" and HAZ is shown on **Fig. 3**. Four distinctive structural areas are revealed namely: (a) zone A of light contrast showing remelted electrode material, (b) zone B of uniformly gray contrast, (c) zone C with heterogeneous structure comprising the areas with grey contrast and dark contrast and (d) zone D located from both sides to the depth of about 1.3 mm having mostly dark contrast (the latter was presumably resulted from decarburization during the manufacturing of steel strip).

Results of microhardness measurement of HAZ (C, B) through fusion layer from indent 1 (zone C) to indent 2 (zone A) are shown on **Fig. 4**.

As seen from the **Fig. 4**, the microhardness of indent 1 is 320 HV, then it varies in the range of 240-260 HV in zone B and 240-270 HV in zone A. Sharp increase in microhardness up to 450 HV is noted for narrow layer located between zone B and zone A.

DOI 10.12776/ams.v25i2.1269 p-ISSN 1335-1532
e-ISSN 1338-1156

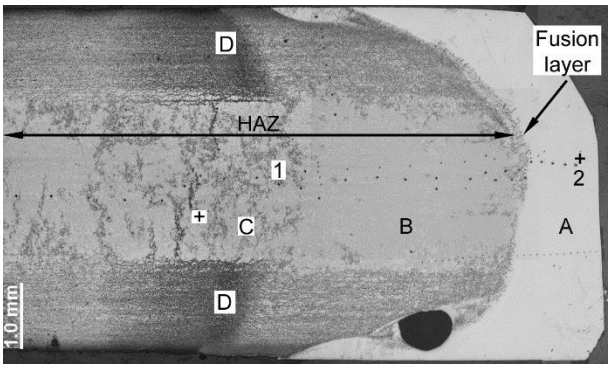

Fig. 3 Panorama of microstructure of HAZ, fusion layer and remelted electrode metal

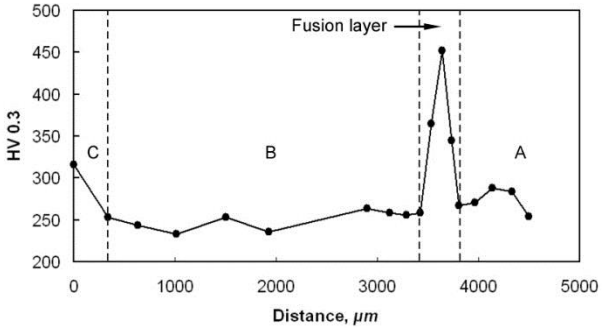

Fig. 4 Results of microhardness measurement of HAZ, fusion layer and remelted electrode metal

The higher microhardness (320 HV) corresponding to indent 1 in zone C is explained by the presence of heterogeneous structure composed of retained austenite, needle martensite and some portion of nodular carbides (shown as "1" in **Fig. 5, a**). According to microhardness value retained austenite is presumably major phase in the structure of zone C while carbides appeared in HAZ due to austenite decomposition under heat input. In contrast of zone C, the microstructure of zones B (**Fig. 5, b**) and A (**Fig. 5, c**) is fully austenitic which is in accordance with its lower microhardness. However, in fusion layer between zones A and B the needle martensite is revealed again (**Fig. 5, d**) resulting in sharp microhardness increase.

As follows from microstructure observation (see **Fig. 3**), martensite presents in significant amount in zone C and it is almost absent in zone B. Therefore the question arises why martensite presenting in zone C suddenly disappears in zone B making clearly visible "border" between theses areas?

The most obvious reason is supposed to be connected with temperature distribution in workpiece under welding heat input. If we assume the exponential mode of temperature distribution in zone B like that on the workpiece surface (see **Fig. 2**) then in zone B temperature rose to higher values than in zone C, to be above Ac_m temperature. Very fast heating suppressed the precipitation of carbides from retained austenite thus retained austenite reached high temperature domain (above Ac_m, **Fig. 6**) without depletion in carbon.

DOI 10.12776/ams.v25i2.1269 p-ISSN 1335-1532
e-ISSN 1338-1156

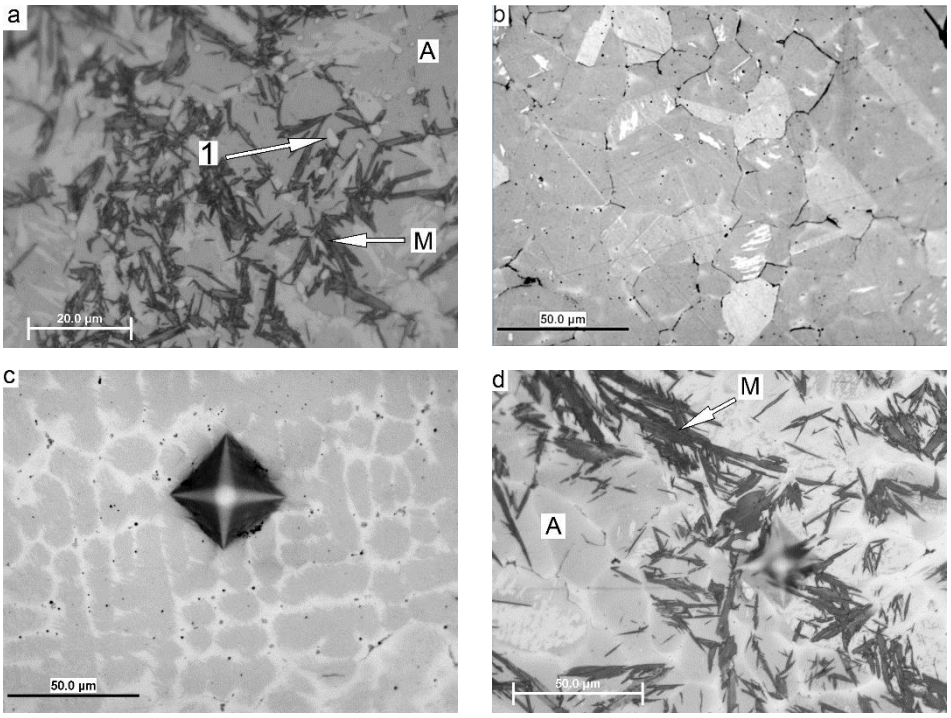

Fig. 5 Microstructure of different zones: (a) zone C; (b) zone B in the vicinity of fusion layer; (c) zone A near penultimate hardness imprint and (d) fusion layer. (Martensite (M), austenite (A) and carbides (1))

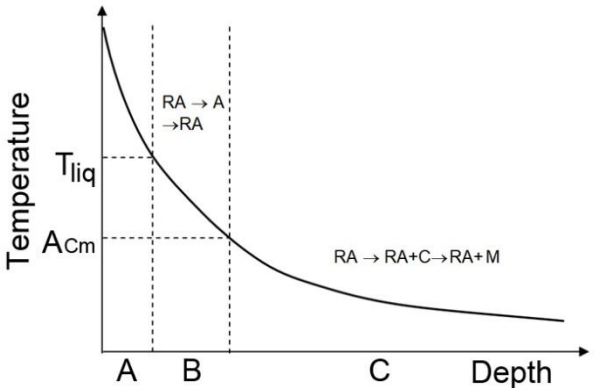

Fig. 6 Schematic temperature distribution in workpiece from model welding joint inward and corresponded structural zones A, B and C (designations RA, C, M are retained austenite, carbide, martensite accordingly)

Under consequent fast cooling this austenite fully retained in the structure forming zone B. In zone C the temperature was below Ac_m to be enough for carbide precipitation from retained austenite. This process resulted in Ms point rising which leads to partial transformation of austenite into martensite in zone C during subsequent cooling.

DOI 10.12776/ams.v25i2.1269 p-ISSN 1335-1532
e-ISSN 1338-1156

This assumption is revealed by the difference in volume fraction of carbide phase between zones C and B shown in **Fig. 7**. **Fig.7a** depicts the carbides as nodular inclusions and as network along grain boundaries which is characteristic for zone C. In contrast, in Fig. **7b** carbide network is not detected while nodular carbides are present; this case corresponds to the boundary between zone C and zone B. That means that less carbides precipitated form austenite under weld cycle when moving from zone C to weld.

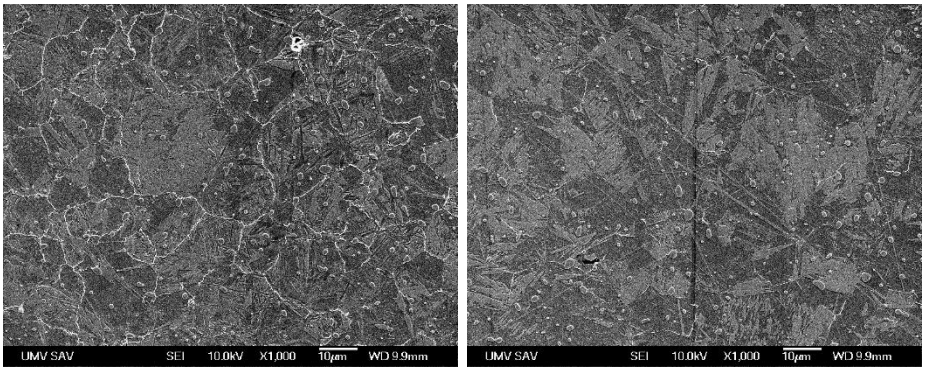

a b

Fig. 7 Microstructure of transition area from zone C to B: (a) near indent 1 (see **Fig. 3**); (b) on the boundary between zone C and zone B

Panorama of transition from zone B to A through the fusion layer is shown on **Fig. 8.** The magnification is the same as of **Fig. 7**. There are no excessive carbides visible in structure. This proves the assumptions concerning heat influence on structure of HAZ that is expressed above. Appearance of martensite in structure of fusion layer (see **Fig. 5, d**) may be explained by the same considerations as for HAZ. The main reason is local rising of Ms due to decarburizing ("dilution") of base metal in fusion layer under melting of electrode material. Excessive alloying of electrode metal by Mn, Cr, Ni may compensate carbon loss and prevent appearance of martensite in fusion layer however this would significantly increase electrodes production costs. Therefore chemical composition of electrode metal should minimally differ from base metal.

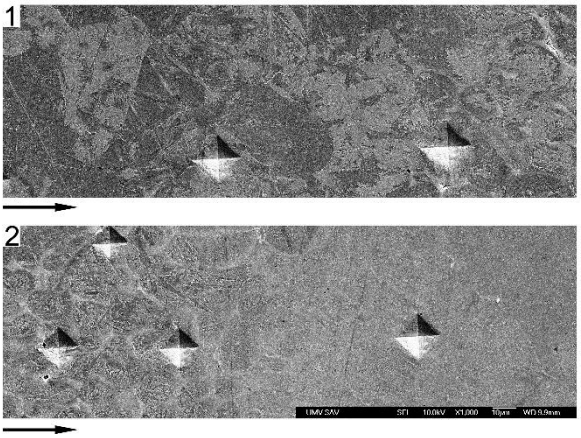

Fig. 8 Microstructure of transition area from zone B to A

DOI 10.12776/ams.v25i2.1269 p-ISSN 1335-1532
e-ISSN 1338-1156

Results of point EDX analyses of base metal and electrode remelted metal are shown on **Fig. 9**. Points of analyses are shown on **Fig. 3** as crosses. According to EDX both base and electrode metals contains approximately equal amount of manganese and silicon, but electrode metal contains 1.5% less of carbon and about 2% of chrome. Detected high values for carbon content should not be taken into account as it is an artifact connected with carbon contamination, which is known weak feature of EDS method. The result of EDX analyses through fusion layer is shown on **Fig. 10**. It is seen that concentration of manganese is approximately the same for base and electrode metal while concentration of chrome rises significantly from base to electrode metal. This result corresponds to that shown on **Fig. 9**.

Spectrum: Spectrum

El	AN	Series	unn. C [wt.%]	norm. C [wt.%]	Atom. C [at.%]	Error (1 Sigma) [wt.%]
C	6	K-series	7,65	7,96	28,36	1,58
Si	14	K-series	1,35	1,40	2,13	0,10
Mn	25	K-series	2,24	2,33	1,81	0,13
Fe	26	K-series	84,93	88,31	67,69	2,58
		Total:	96,17	100,00	100,00	

a

Spectrum: Spectrum

El	AN	Series	unn. C [wt.%]	norm. C [wt.%]	Atom. C [at.%]	Error (1 Sigma) [wt.%]
C	6	K-series	6,26	6,55	24,31	1,41
Si	14	K-series	1,11	1,16	1,84	0,09
Cr	24	K-series	2,14	2,24	1,92	0,12
Mn	25	K-series	2,34	2,44	1,98	0,14
Fe	26	K-series	83,78	87,61	69,94	2,56
		Total:	95,63	100,00	100,00	

b

Fig. 9 Results of EDX analyses of base metal (a) and electrode remelted metal (b)

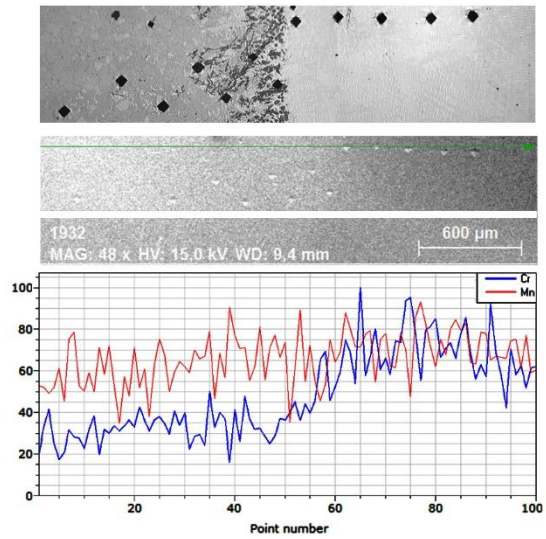

Fig. 10 Result of EDX analyses of Cr and Mn perpendicularly to fusion line

The results obtained allow concluding that rapid cooling is promising way to preserve initial wear resistant structure of retained austenite in HAZ of high-carbon low-alloyed steels during arc welding. Further investigations may be conducted to develop suitable techniques for providing rapid cooling in course of welding different machine parts produced from such steels.

4 Conclusions

Investigation of structure and chemical composition of fusion layer and heat affected zone of high-carbon low-alloyed wear resistant steel quenched to retained austenite after welding leads to following conclusions.

DOI 10.12776/ams.v25i2.1269 p-ISSN 1335-1532
e-ISSN 1338-1156

1. Rapid cooling of welding join is useful to obtain in HAZ fully austenitic structure that is identical to initial structure of as-quenched steel. Rapid cooling is also needed to avoid or minimize precipitation of carbides from austenite thus preventing appearance of martensite in HAZ.
2. Chemical composition of electrode metal should be adjusted in order to eliminate hardness gradient in structure of fusion line.

References

[1] Sarveshwar M. Reddy, Nikhil Sharma, Neeraj Gupta, Avinash Kumar Agarwal: Fuel, Vol. 222, 2018, p. 841-851, https://doi.org/10.1016/j.fuel.2018.02.132
[2] M. Džupon, L. Kaščák, E. Spišák, R. Kubík, J. Majerníková: Metals, Vol. 7, 2017, No. 11, p. 515, https://doi.org/10.3390/met7110515
[3] L. Kaščák, J. Mucha, E. Spišák, R. Kubík: Strength of Materials, Vol. 49, 2017, No. 5, p. 726-737, https://doi.org/10.1007/s11223-017-9918-9
[4] R. Kubík, L. Kaščák, E. Spišák: Koroze a Ochrana Materialu, Vol. 60, 2016, No. 5, p. 154-161, https://doi.org/10.1515/kom-2016-0025
[5] E.V. Sukhovaya: Journal of Superhard Materials, Vol. 35, 2013, No. 5, p. 277-283, https://doi.org/10.3103/S106345761305002X
[6] R. Lencina, C. Caletti, K. Brunelli, R. Micone: Procedia Materials Science, Vol. 9, 2015, p. 358-366, https://doi.org/10.1016/j.mspro.2015.05.005.
[7] J. Viňáš, L. Kaščák: Bulletin of Materials Science, Vol. 31, 2008, No. 2, p. 125–131, https://doi.org/10.1007/s12034-008-0022-4
[8] J. Brezinová, D. Draganovská, A. Guzanová, P. Balog, J. Viňáš: Metals, Vol. 6, 2016, No. 2, p. 36, https://doi.org/10.3390/met6020036
[9] J. Viňáš et al.: Materials Science Forum, Vol. 862, 2016, p. 41-48
[10] M. Orečný, M. Buršák, J. Viňáš.: Metalurgija, Vol. 54, 2015, No. 1, p. 191-193
[11] L. S. Malinov, V. L. Malinov, D. V. Burova, V. V. Anichenkov: Journal of Friction and Wear, Vol. 36, 2015, No. 3, p.237–240, https://doi.org/10.3103/S1068366615030083
[12] V.G. Efremenko et al.: Journal of Friction and Wear, Vol. 34, 2013, No. 6, p. 466–474, https://doi.org/10.3103/S1068366613060068
[13] A.V. Makarov, L.G. Korshunov, I.Yu. Malygina, I.L. Solodova.: Metal Science and Heat Treatment, Vol. 49, 2007, No. 3-4, p.150-156, https://doi.org/10.1007/s11041-007-0028-3
[14] M. Šebek, F. Kováč, I. Petryshynets, J. Balko: Materials Science Forum, Vol. 891, 2017, p. 171-175, https://doi.org/10.4028/www.scientific.net/MSF.891.171
[15] M. Šebek, L. Falat, F. Kováč, I. Petryshynets, P. Horňak, V. Girman: Archives of Metallurgy and Materials, Vol. 62, 2017, No. 3, p. 1721-1726, https://doi.org/10.1515/amm-2017-0262
[16] M. Šebek, L. Falat, M. Orečny, I. Petryshynets, F. Kovác, M. Černík: International Journal of Materials Research, Vol. 109, 2018, No. 5, p. 460-468, https://doi.org/10.3139/146.111624
[17] O. Hesse, J. Merker, M. Brykov, V. Efremenko: Tribologie und Schmierungstechnik, Vol. 60, 2013, No. 6, p. 37-43
[18] O. Hesse, J. Liefeith, M. Kunert, A. Kapustyan, M. Brykov, V. Efremenko: Tribologie und Schmierungstechnik, Vol. 63, 2016, No. 2, p. 5-13
[19] V.G. Efremenko et al.: Wear, Vol. 418–419, 2019, p. 24-35, https://doi.org/10.1016/j.wear.2018.11.003
[20] Hong Liang Li, Duo Liu, YanYu Song, YaoTian Yan, Ning Guo, JiCai Feng: Journal of Materials Processing Technology, Vol. 249, 2017, p. 149-157, https://doi.org/10.1016/j.jmatprotec.2017.06.009

[21] Şükrü Talaş: Materials & Design (1980-2015), Vol. 31, 2010, No. 5, p. 2649-2653, https://doi.org/10.1016/j.matdes.2009.11.066
[22] H. Bhadeshia, R. Honeycombe: *Steels: Microstructure and Properties*, fourth ed., Elsevier, 2017
[23] A. Devaraju, V. Kishan: Materials Today: Proceedings, Vol. 5, 2018, No. 1, Part 1, p. 1585-1590, https://doi.org/10.1016/j.matpr.2017.11.250
[24] A. Devaraju: Materials Today: Proceedings, Vol. 4, 2017, No. 2, Part A, p. 3722-3727, https://doi.org/10.1016/j.matpr.2017.02.267
[25] X.C. Liu, Y.F. Sun, T. Nagira, H. Fujii: Materials Characterization, Vol. 137, 2018, p. 24-38, https://doi.org/10.1016/j.matchar.2018.01.004
[26] H. Zhang et al.: Journal of Materials Science & Technology, Vol. 34, 2018, No. 11, p. 2183-2188, https://doi.org/10.1016/j.jmst.2018.03.014
[27] E. Curiel-Reyna, A. Herrera, V. M. Castaño, M. E. Rodriguez: Materials and Manufacturing Processes, Vol. 20, 2005, No. 5, p. 813-822, https://doi.org/10.1081/AMP-200055142
[28] I.A. Bataev et al.: Acta Materialia, Volume 135, 2017, p. 277-289, https://doi.org/10.1016/j.actamat.2017.06.038
[29] A. Ascari, A. Fortunato: Optics & Laser Technology, Vol. 56, 2014, p. 25-34, https://doi.org/10.1016/j.optlastec.2013.07.016.
[30] Hideki Hamatani, Yasunobu Miyazaki, Tadayuki Otani, Shigeru Ohkita: Materials Science and Engineering: A, Vol. 426, 2006, No. 1–2, p. 21-30, https://doi.org/10.1016/j.msea.2006.03.024

Acknowledgements
This work is supported by Slovak Academic Information Agency (SAIA).

EFFECT OF BINDER COMPOSITION AND SINTERING TEMPERATURE ON THE MICROSTRUCTURE AND MECHANICAL PROPERTIES OF WC-7(Ni,Fe) HARD ALLOYS PREPARED BY FREE CAPSULE HIP TECHNIQUE

Doan Dinh Phuong[1], Tran Bao Trung[1,], Le Danh Chung[1], Tran Ba Hung[2]*
[1)]Institute of Materials Science, Vietnam Academy of Science and Technology, No.18, Hoang Quoc Viet Str., Cau Giay Distr., Hanoi, Vietnam
[2)]Center for High Technology Development, Vietnam Academy of Science and Technology, No. 18, Hoang Quoc Viet Str., Cau Giay Distr., Hanoi, Vietnam

Received: 30.05.2019
Accepted: 16.06.2019

[*]Corresponding author: e-mail: trungtb@ims.vast.ac.vn, Tel.: +84912 774 333, Department of Advanced Metallic Materials, Institute of Materials Science, Vietnam Academy of Science and Technology, No.18, Hoang Quoc Viet Str., Cau Giay Distr., Hanoi, Vietnam

Abstract
In this research, WC-7(Ni,Fe) hard alloys were prepared by ball milling, cold compaction and finally consolidated by hot isostatic pressing. The effect of binder composition and sintering temperature were investigated in term of the microstructure, density and mechanical properties of sintered samples. Density of hard alloys was measured by the Archimedes' principle while the microstructure was observed using a scanning electron microscope. The Vickers hardness was investigated at load of 30KG and the fracture toughness was calculated based on the Palmqvist crack method. The results revealed that the density of sintered samples was obtained in the range of 14.65 to 14.8 g/cm^3 meanwhile the measured Vicker hardness and fracture toughness were respectively achieved from 1260 to 1520 HV30 and 11,7 to 17,5 MPa.m$^{1/2}$ depending on the binder composition and sintered temperature.

Keywords: hard alloys, hot isostatic pressing, Vickers hardness, fracture toughness

1 Introduction

WC based hard alloys have been used in a wide range of applications including metal cutting tools, mining tools, wear resistant parts and wire-drawing dies [1-5]. Since the invention of WC hard alloys, Co metal has been the most optimum binder phase for producing these kinds of materials due to its good wettability to WC grains and high mechanical properties which bring to the remarkable properties of WC-Co hard alloys such as high hardness and toughness [5-8]. However, several drawbacks of using Co binder for WC hard alloys have been found such as low corrosion-, oxidation-resistance and the raising the suspects of harmful effects to human body concerning to WC-Co containing dust [3, 7-10]. Moreover, the high price and limitation of Co resource have to be taken into consideration. Recently, efforts have been paid to find out new binder alloys to replace Co in WC hard alloys in which Ni, Fe and their alloys have been considered as the ideal binders for WC hard alloys [2-7, 10-11]. The substitution of Co by Ni and Fe has been investigated in literature. The results showed that the Fe/Ni ratio plays an important role in the microstructure and properties of WC-Co-Fe-Ni hard alloys. The increase of Fe/Ni ratio would bring to the binder phase consisting of γ-(Fe,Ni), α-(Fe,Ni) or mixture of these two phases and subsequently, effected

DOI 10.12776/ams.v25i2.1270 p-ISSN 1335-1532
e-ISSN 1338-1156

on the mechanical properties of WC-Co-Fe-Ni hard alloys [11]. The WC-Co-Fe-Ni hard alloys exhibited optimal properties when the binder phase was fcc structure [11-12]. The toughness of WC-(Fe,Ni) alloys could be improved using a suitable heat treatment and controlling the carbon content [13]. In addition, the corrosion resistance of WC-15(Fe,Ni) was considered to be better than WC-15Co alloy [14]. The results above show that Fe-Ni binder is considered to be a potential binder to replace Co for production of WC hard alloys. In this research, WC-7(Ni,Fe) alloys are fabricated using the hot isostatic pressing technique, an advanced technique to consolidate WC based hard metals [15-16]. The effect of Fe content and sintering temperature on the microstructure and mechanical properties will be brought out for discussions.

2 Experimental procedure

The raw powders used in this work were WC (< 3 µm, TaeguTec Co.), Ni (<5 µm, TaeguTec Co.) and Fe (<50 µm, Xilong scientific Co., Ltd.). The SEM images of raw powders are shown in **Fig. 1a,b,c**. The composition of hard alloys was designed for WC-7(Fe,Ni) in which Fe content was varied from 0 to 3 wt.%. The sample codes and composition are shown in **Table 1**. The hard alloy powders were produced by ball milling in n-hexane medium for 72 h using the WC-Co balls and jar. The ball to powder ratio was 6:1. The as-milled powders were then reduced in hydrogen gas flow for 4 h at 500 °C to eliminate the metal oxides formed during the ball milling. After the

Table 1 Sample composition of designed hard alloys

Sample code	WC-7Ni	WC-6Ni1Fe	WC-5.5Ni1.5Fe	WC-5Ni2Fe	WC-4.5Ni2.5Fe	WC-4Ni3Fe
Ni content (wt.%)	7	6	5.5	5	4.5	4
Fe content (wt.%)	0	1	1.5	2	2.5	3

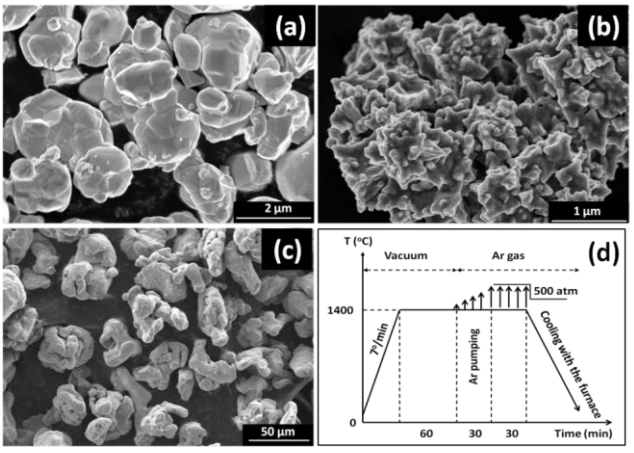

Fig. 1 SEM images of raw powders a)WC, b) Ni and d) Fe, and d) sintering scheme for samples.

hydrogen reduction process, the mixture powders were subsequently mixed with 2 wt.% paraffin wax as the pressing aid. The cold compaction was done in a cylindrical mould of 13 mm in diameter at the pressure of 1 ton.cm^{-2}. The obtained pellets were pre-heat treated at 800 ^{o}C for 1 h

DOI 10.12776/ams.v25i2.1270 p-ISSN 1335-1532
e-ISSN 1338-1156

in Ar gas to eliminate the pressing aid and other organics contaminated in the samples. The pellets were sintered by free capsule hot isostatic pressing at different sintered temperatures. The sintering procedure was carried out as seen in **Fig. 1d** in which the samples were heated up to sintered temperature and kept at this temperature for 1 h in vacuum; the Ar gas was then pumped into the sample chamber to the pressure of 500 atm and held at this pressure for 30 min and subsequently, cooled to room temperature. The sintered samples were measured the density using Archimedes' principle. Phase component was analyzed by X-rays diffraction (XRD, Advanced Bruker, D5005) meanwhile the microstructure was observed using field emission scanning electron microscope (FE-SEM, Hitachi S4800). The mechanical properties were investigated in term of Vicker hardness, HV30 (Mitutoyo AVK-C0) and fracture toughness, K_{IC} based on Palmqvist crack method [17-19].

3 Results and discussion

3.1 The effect of Fe content

The effect of binder composition on the phase formation of samples sintered at 1400°C was analyzed based on the XRD patterns as shown in **Fig. 2**. In the sample without Fe (WC-7Ni), the main obtained phases are WC and Ni metal. When Ni was partially alternated by Fe, the results revealed the diffraction peaks of two phases; WC and γ-(Ni,Fe). Individual phases of Ni and Fe were not observed. This implied that the solid solution of NiFe was formed during sintering. Besides that the peaks of η-phase, $(W,Ni,Fe)_6C$, were not detected for all compositions, even with the sample containing 3 wt.% Fe. This assumes that the C content may be in the range of two-phase region [13, 20-21].

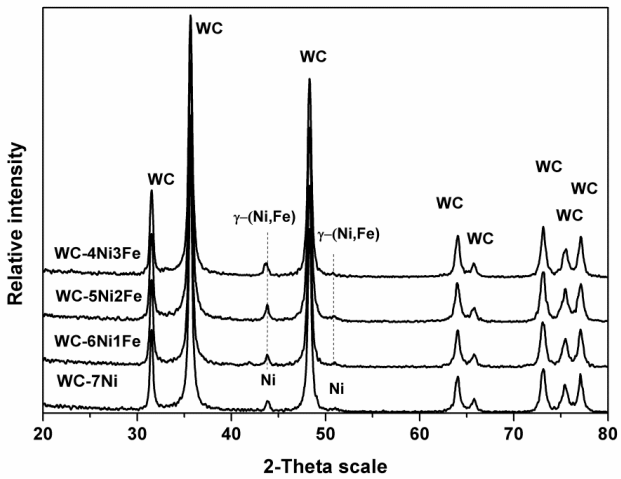

Fig. 2 XRD patterns of sintered samples with different composition.

Microstructure of sintered hard alloys was observed by FE-SEM equipment using back scattered electron mode as seen in **Fig. 3**. The bright colors, gray colors and black colors are WC, NiFe and micropores, respectively. The observed micropores in all specimens could be attributed to the insufficient sintered temperature and time or due to the low Ar gas pressure of HIP process. The measured densities of sintered samples are presented in **Fig. 4a**. It shows that the density of hard alloys decreased from 14.71 to 14.41 g/cm^3 as the amount of Fe increased from 0 to 3 wt.%. This

DOI 10.12776/ams.v25i2.1270 p-ISSN 1335-1532
e-ISSN 1338-1156

is attributed to the lower density of Fe in comparison with the density of Ni metal. The appearance of pores leads to the decrease of the mechanical properties, especially for the toughness. The measured Vickers hardness and fracture toughness of sintered hard alloys are shown in the **Fig. 4b**. It is obviously to see the increase of Vickers hardness with the increase of Fe content. The Vickers hardness was about 1260 HV30 for the sample without Fe and then gradually increased to about 1520 HV30 for the sample using 3 wt.% Fe. Previous studies revealed that the hardness of hard alloys depend on the WC grain size, binder amount and binder structure. As the Fe content increased, the γ solid solution of Ni and Fe was changed and resulted in the increase of the hardness. The fracture toughness, however, has a trend to decrease with the increase of Fe content. The maximum value of K_{IC} was reached at 17.6 MPa.m$^{1/2}$ in the sample WC-7Ni and reduced to 11.7 MPa.m$^{1/2}$ in the WC-4Ni3Fe sample.

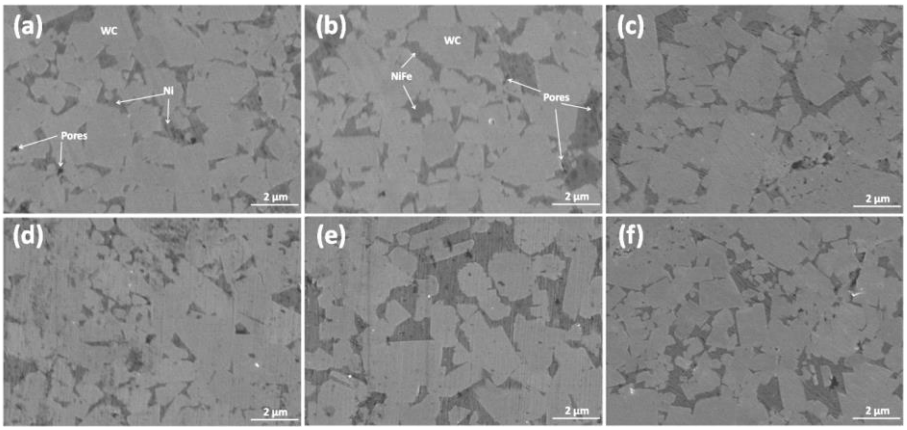

Fig. 3 FE-SEM images of; a) WC-7Ni, b) WC-6Ni1Fe, c) WC-5.5Ni-1.5Fe, d) WC-5Ni2Fe, e) WC-4.5Ni2.5Fe and f) WC-4Ni3Fe

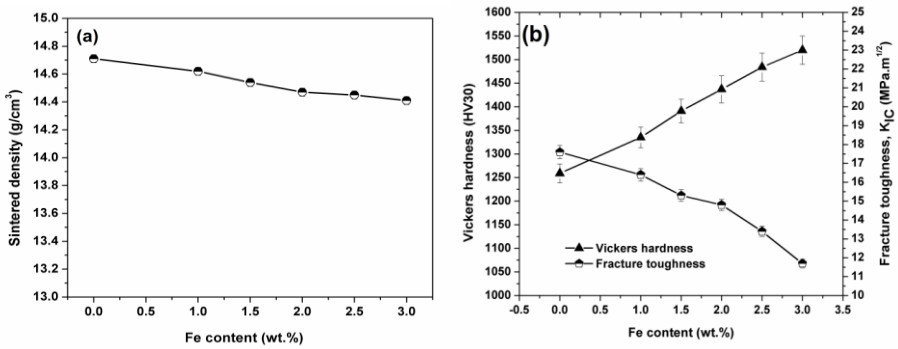

Fig. 4 Effect of Fe content on; a) density and b) mechanical properties of WC-7(Ni,Fe) alloys

3.2 Effect of sintering temperature

In order to investigate the effect of sintering temperature, the samples with composition of WC-6Ni1Fe were sintered at different temperatures; 1400, 1410, 1420 and 1440 °C using the same sintering schedule as presented in **Fig. 1d**. **Fig. 5** shows the XRD patterns of WC-6Ni1Fe hard alloys sintered at variety of temperatures. From **Fig. 5**, only diffraction peaks of WC and γ-(Ni,Fe)

DOI 10.12776/ams.v25i2.1270 p-ISSN 1335-1532
e-ISSN 1338-1156

was observed in all samples, no η-phase or other phases was detected. The effect of sintering temperatures can be seen via the intensity of γ-(Ni,Fe) diffraction peaks. As the sintering temperature increased, the intensity of these peaks was greater which might be resulted from the growth of γ-(Ni,Fe) crystalline. **Fig. 6** shows the FE-SEM images of sintered samples. With the increase of temperature, the liquid phase of γ-(Ni,Fe) was more flexible to fill into the spaces between the WC particles and provided a higher driving force for consolidation of hard alloys during sintering. The FE-SEM images also show the grain growth and coarsening phenomenon of WC with the raising of sintered temperature. The density of sintered samples is presented in **Fig.7a**. A higher density was achieved at higher sintered temperature. The highest density was achieved at about 14.8 g/cm^3 for sample sintered at 1440 °C. It is close to the theoretical density calculated for WC-6Ni1Fe composition (14.813 g/cm^3). This shows that the HIP sintering technique can be used to consolidate these hard alloys to the full density.

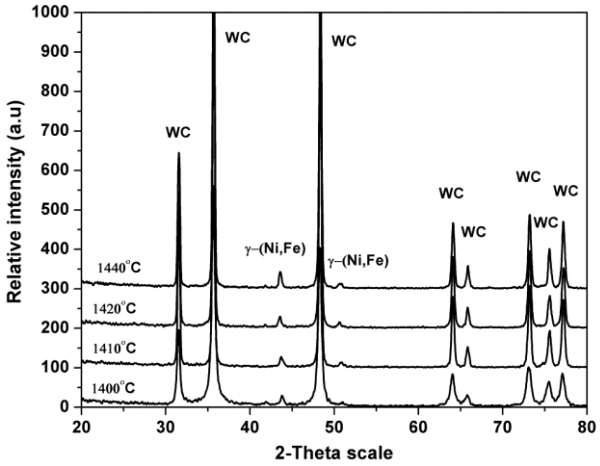

Fig. 5 XRD patterns of WC-6Ni1Fe sintered at different temperatures

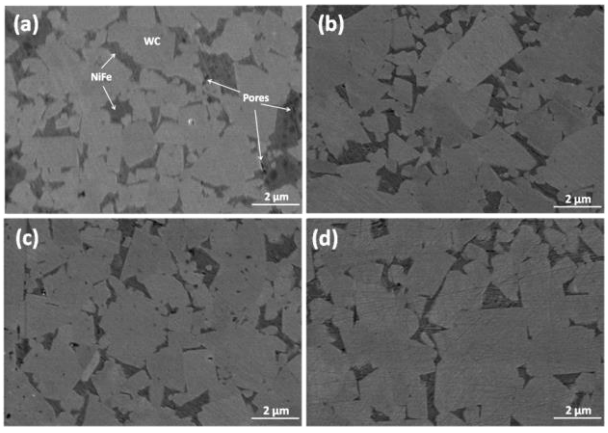

Fig. 6 FE-SEM images of WC-6Ni1Fe hard alloys sintered at; a)1400°C, b) 1410°C, c) 1420°C and d) 1440°C

Fig. 7b shows the effect of sintering temperature of the Vickers hardness and fracture toughness of WC-6Ni1Fe alloys. The Vicker hardness and fracture toughness increased from about 1335 to

DOI 10.12776/ams.v25i2.1270 p-ISSN 1335-1532
e-ISSN 1338-1156

1378 HV30 and from 16.4 to 16.6 MPa.m$^{1/2}$, respectively, as temperature increased from 1400°C to 1410°C. And then, the hardness of alloys had a tendency to decrease whilst the fracture toughness continually increased to 17.1 MPa.m$^{1/2}$ with further increase of sintering temperature. The improvement of hardness of sample consolidated at 1410 °C was due to the higher density and the elimination of pores in the microstructure of hard alloy. Thereafter, the grain growth of WC was enhanced with the higher temperatures leading to the reduction of hardness following the Hall-Petch relationship [22-23]. The enhancement of fracture toughness was attributed to the better consolidation and grain growth of WC with the increase of sintering temperature.

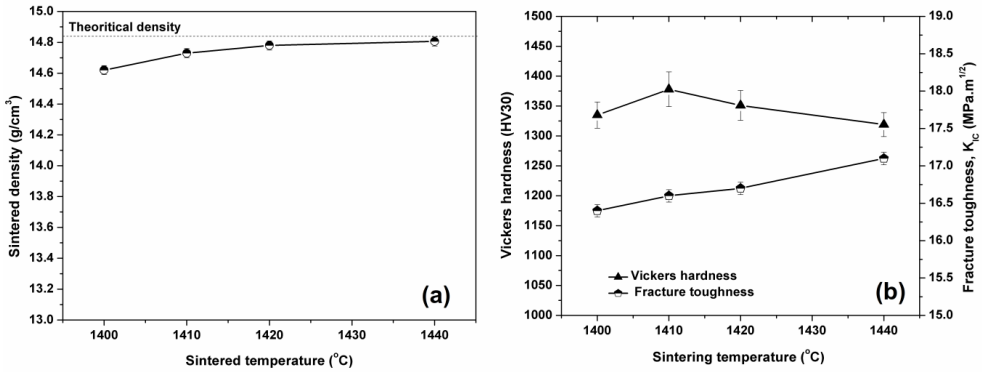

Fig. 7 Effect of sintering temperature on a) density and b) mechanical properties of WC-6Ni1Fe

4 Conclusion

In this work, WC-7(Ni,Fe) hard alloys have been fabricated via the powder metallurgy technology using hot isostatic pressing method. The results revealed that the mechanical properties of hard alloys strongly depended on the binder composition and sintering temperature. The replacement of Ni by Fe leaded to the improvement of hardness but also resulted in the reduction of fracture toughness. Increasing the sintering temperature leaded to the improvement of hard alloys' density and WC grain growth and therefore resulted in the enhancement of fracture toughness. The highest density and fracture toughness were reached at 14.8 g/cm^3 and 17.1 MPa.m$^{1/2}$, respectively, for the sample sintered at 1440 °C. However, the highest Vickers hardness value of 1378 HV30 was obtained for the sample sintered at 1410 °C and then, reduced with higher sintered temperature due to the grain growth of WC.

Referrences

[1] A. Mukhopadhyay, B. Basu: Journal of Materials Science, Vol. 46, 2011, p. 571–589, https://doi.org/10.1007/s10853-010-5046-7

[2] V. A. Tracey, International Journal of Refractory Metals and Hard Materials, Vol. 11, 1992, No. 3, p.137-149, https://doi.org/10.1016/0263-4368(92)90056-8

[3] H. Rong, Z. Peng, X. Ren, Y. Peng, C. Wang, Z. Fu, L. Qi, H. Miao: Material Science Engeneering: A, Vol. 532, 2012, p. 543– 547, https://doi.org/10.1016/j.msea.2011.10.119

[4] H. C. Kim, I. J. Shon, J. K. Yoon, J. M. Doh, Z. A. Munir: International Journal of Refractory Metals and Hard Materials, Vol. 24, 2006, p. 427–431, https://doi.org/10.1016/j.ijrmhm.2005.07.002

[5] R. K. Viswanadham &P. G. Lindquist: Metallurgical Transactions A, Vol. 18, 1987, No. 12, p. 2163–2173, https://doi.org/10.1007/bf02647089

DOI 10.12776/ams.v25i2.1270 p-ISSN 1335-1532
e-ISSN 1338-1156

[6] D. H. Xiao, Y. H. He, M. Song, N. Lin, R. F. Zhang: International Journal of Refractory Metals and Hard Materials, Vol. 28, 2010, No. 3, p. 407–411, https://doi.org/10.1016/j.ijrmhm.2009.12.008
[7] C. M. Fernandes & A. M. R. Senos: International Journal of Refractory Metals and Hard Materials, Vol. 29, 2011, No. 4, p. 405–418, https://doi.org/10.1016/j.ijrmhm.2011.02.004
[8] M. D. Boeck, M. Kirsch-Volders, D. Lison: Mutation Research-Fundamental and Molecular Mechanisms of Mutagenesis, Vol. 533, 2003, p. 135-152, https://doi.org/10.1016/j.mrfmmm.2003.07.012
[9] A. Daniel, K. V. Micheline, E. Azeddine, B. Kathy, L. Dominique: Carcinogenesis, Vol. 18, 1997, No.1, p.177–184, https://doi.org/10.1093/carcin/18.1.177
[10] L. St-Georges: Wear, Vol. 263, 2007, Iss. 1–6, p. 562-566, https://doi.org/10.1016/j.wear.2007.02.023
[11] Y.Gao, B. H. Luo, K. J. He, W. W. Zhang, Z. H. Bai: Ceramic International, Vol. 44, 2018, p. 2030–2041, https://doi.org/10.1016/j.ceramint.2017.10.148
[12] Y. Gao, B. H. Luo, K. Jian He, H. B. Jing, Z. H. Bai, W. Chen, W. W. Zhang: Vacuum, Vol. 143, 2017, p. 271-282, https://doi.org/10.1016/j.vacuum.2017.06.028
[13] R. Gonzalez, J. Echeberria, J. M. Sanchez, F. Castro: Journal of Materials Science, Vol. 30, 1995, p. 3435-3439, https://doi.org/10.1007/BF00349891
[14] S. H. Chang, S. L. Chen: Journal of Alloys and Compounds, Vol. 585, 2014, p. 407–413, https://doi.org/10.1016/j.jallcom.2013.09.188
[15] C. M. Fernandes, A. M. R. Senos, M. T. Vieira, J. M. Antunes: International Journal of Refractory Metals & Hard Materials, Vol. 26, 2008, p. 491–498, https://doi.org/10.1016/j.ijrmhm.2007.12.001
[16] I. Azcona, A. Ordóñez, J. M. Sánchez, F. Castro: Journal of Materials Science, Vol. 37, 2002, No. 19, p. 4189–4195, https://doi.org/10.1023/A:1020048105585
[17] A. M. Soleimanpour, P. Abachi, A., Simchi: International Journal of Refractory Metals and Hard Materials, Vol. 31, 2012, p. 141-146. https://doi.org/10.1016/j.ijrmhm.2011.10.004
[18] D. K. Shetty, I. G. Wright, P. N. Mincer, A. H. Clauer: Journal of Materials Science, Vol. 20, 1985, p.1873-1882, https://doi.org/10.1007/BF00555296
[19] B. E. Meacham, M. C. Marshall, D. J. Branagan: Metallurgical and Materials Transaction A, Vol. 37A, 2006, p. 3617-3627, https://doi.org/10.1007/s11661-006-1056-0
[20] B. Uhrenius, H. Pastor, E. Pauty: International Journal of Refractory Metals and Hard Materials, Vol. 15, 1997, p. 139-149, https://doi.org/10.1016/S0263-4368(96)00023-6
[21] R. Bidulsky, J. Bidulska, F. Arena, M. Actis Grande: High Temperature Materials and Processes, Vol. 31, 2012, Iss. 1, p. 13-17
[22] R. Furushima, K. Katou, K. Shimojima, H. Hosokawa, A. Matsumoto: International Journal of Refractory Metals and Hard Materials, Vol. 50, 2015, p. 16–22, https://doi.org/10.1016/j.ijrmhm.2014.11.007
[23] R. W. Armstrong: Materials, Vol. 4, 2011, p. 1287-1308; https://doi.org/10.3390/ma4071287

Acknowledgment

The authors gratefully acknowledge to the Vietnam Academy of Science and Technology for the financial support of this research under the project No. VAST.TD.QP.02/17-19.

COMPARISON OF SALT BATH PREOXIDATION AND AIR PREOXIDATION FOR SALT BATH NITRIDING

Wenchen Mei[1)], Jiqiang Wu[1,2)], Mingyang Dai[1)], Kunxia Wei[1)],Jing Hu[1,2)]*
[1)] School of Materials Science and Engineering, Jiangsu Key Laboratory of Materials Surface Science and Technology, Changzhou University, Changzhou 213164, China
[2)] Sinopec Oilfield Equipment Corporation Kingdream Public Limited Company, Wuhan 430223, China

Received: 09.04.2019
Accepted: 17.06.2019

**Corresponding author: Jing Hu, e-mail: jinghoo@126.com, School of Materials Science and Engineering, Jiangsu Key Laboratory of Materials Surface Science and Technology, Changzhou University, Changzhou 213164, China*

Abstract
Salt bath preoxidation was primarily conducted prior to salt bath nitriding, and the effect on salt bath nitriding was compared with that of conventional air preoxidation. Characterization of the modified surface layer was made by means of optical microscopy, scanning electron microscope (SEM), micro-hardness tester and x-ray diffraction (XRD). The results showed that the salt bath preoxidation could significantly enhance the nitriding efficiency. The thickness of compound layer was increased from 13.3μm to 20.8μm by salt bath preoxidation, more than 60% higher than that by conventional air preoxidation under the same salt bath nitriding parameters of 560℃ and 120min. Meanwhile, higher cross-section hardness and thicker effective hardening layer were obtained by salt bath preoxidation, and the enhancement mechanism of salt bath preoxidation was discussed.

Keywords: peroxidation, salt bath nitriding, microstructure, hardness

1 Introduction

Salt bath nitriding is a kind of valuable chemical heat treatment widely used for steels to obtain the required properties [1-3]. Compared with other nitriding technologies, salt bath nitriding has obvious advantages, such as with better quality and lower cost [4-6]. After salt bath nitriding, a compound layer is formed, which can significantly improve the performance of metal [7-9]. However, for obtaining the effective thickness of nitrided layer, the nitriding temperature or holding time must be increased [10-12], which would bring out porosity in the nitrided layer, thus may results in side effect on the surface hardness and wear resistance.

It has been reported that preoxidation can enhance the nitriding efficiency, since a thin oxide layer is formed during preoxidation process, which can be decomposed during the followed nitriding process [13, 14]. Traditionally, preoxidation process is conducted in air furnace before salt bath nitriding [15, 16]. Unfortunately, it is found that air preoxidation has little enhancement effect on salt bath nitriding [17, 18].

Based on the efficiency of salt bath nitriding is much higher than that of gas nitriding, it is valuable to study if salt bath oxidation could have much better enhancement effect on salt bath nitriding. Therefore, the goal of this research is to investigate if salt bath oxidation can bring out much better enhancement effect on salt bath nitriding than that of conventional air preoxidation.

DOI 10.12776/ams.v25i2.1271 p-ISSN 1335-1532
e-ISSN 1338-1156

2 Experimental

AISI 1045 steel was selected as the substrate material with the chemical composition (wt.%) of: 0.46 C, 0.17 Si, 0.52 Mn, 0.24 Cu,0.21 Ni, 0.23 Cr, 0.022 S,0.023 P, and balance Fe. The specimens were machined into a size of 10mm×10mm×10 mm, followed by quenching at 860℃and tempering at 600℃ to get uniform microstructure. Then the mechanically polished specimens were treated with emery papers of different granulometry (240, 500, 1500 and 2000 mesh) to achieve a mirror finish. Finally, the specimens were ultrasonically cleaned in anhydrous ethanol and dried before salt bath nitriding treatment. The major chemical constituents of preoxidation salt bath medium are sodium hydroxide (NaOH), sodium nitrate ($NaNO_3$) and sodium carbonate (Na_2CO_3).

The main treating process was composed of three steps: preoxidation, salt bath nitriding and cooling. Firstly, the samples were preoxidation to 35°C for different time (45, 60min) in air furnace or in salt bath oxidation medium and then nitrided in salt bath nitriding medium at 560°C for 120min. Finally, samples were cooled in water.

The cross sectional microstructure was observed by optical microscopy and the surface of samples was observed by scanning electron microscopy (SEM). Hardness measurements were made in a HXD-1000TMC micro-hardness tester, with the test load of 10g and holding duration of 15s. Each hardness value was determined by averaging at least 5 measurements. The phase constituents were determined by X-ray diffraction (XRD) with Cu-Ka (λ= 1.54 Å) radiation.

3 Results and discussion

3.1 Cross-sectional microstructure and depth analysis

Fig. 1 presents the cross-sectional microstructure of specimens nitrided at 560°C for 120min with different preoxidation method. It clearly shows that compound layer (also called white layer) is formed at the outermost surface after salt bath nitriding under different conditions and the thickness of compound layer is significantly increased by salt bath preoxidation, the thickness of compound layer of 13.3μm by APON is increased to 20.8μm by SPON, more than 60% increased. This indicates the salt bath preoxidation can improve the efficiency of salt bath nitriding.

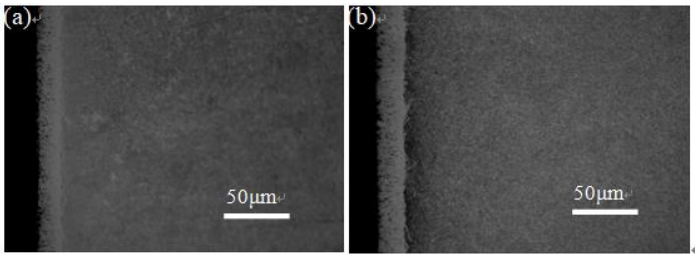

Fig. 1 The cross-sectional microstructure of specimens nitrided at 560℃ for 120min with different preoxidation methods (a) APO 350 ℃×45 min; (b) SPO 350 ℃×45 min

3.2 Micro-hardness profile

Fig. 2 shows the micro-hardness profile of specimens nitrided at 560°C for 120min with different preoxidation methods. It clearly shows that the cross-section micro-hardness can be significantly increased by salt bath nitriding with different preoxidation methods. The specimen treated by SPON has higher cross-section micro-hardness than that treated by APON. Meanwhile, the effective hardening layer thickness, defined as the layer with hardness $50HV_{0.01}$ higher than that

DOI 10.12776/ams.v25i2.1271 p-ISSN 1335-1532
e-ISSN 1338-1156

of substrate, is evidently increased with salt bath preoxidation. This indicates the salt bath preoxidation enhancement effect on salt bath nitriding is greater than air preoxidation.

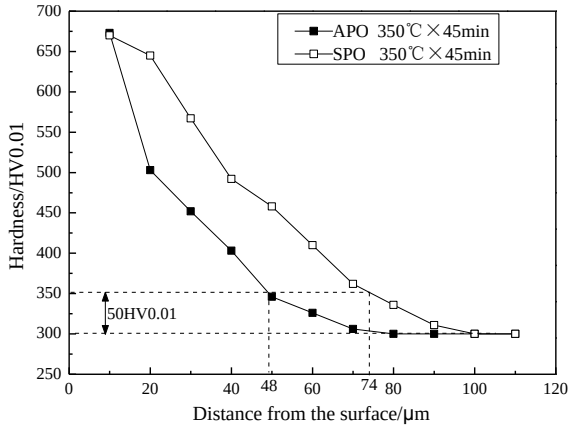

Fig. 2 The micro-hardness profile of specimens nitrided at 560℃ for 120min with different preoxidation methods

3.3 XRD analysis

Fig. 3 shows XRD diffraction patterns of samples after different preoxidation methods. It clearly shows that though Fe_3O_4 phase formed on the surface after different preoxidation process, the relative content of Fe_3O_4 is different, which can be obtained by calculating the ratio of the strongest peak of Fe_3O_4 to the strongest peak of α-Fe [19, 20], and it can be seen that the relative content of Fe_3O_4 treated by salt bath preoxidation is much higher than that treated by air preoxidation. Therefore, the salt bath preoxidation enhancement effect on salt bath nitriding is greater than air preoxidation. Meanwhile, when air preoxidation time increases to 60 min, the Fe_2O_3 phase is formed on the surface, which indicates that too long holding time results in excessive oxidation and is unfavorable for subsequent nitriding [21, 22].

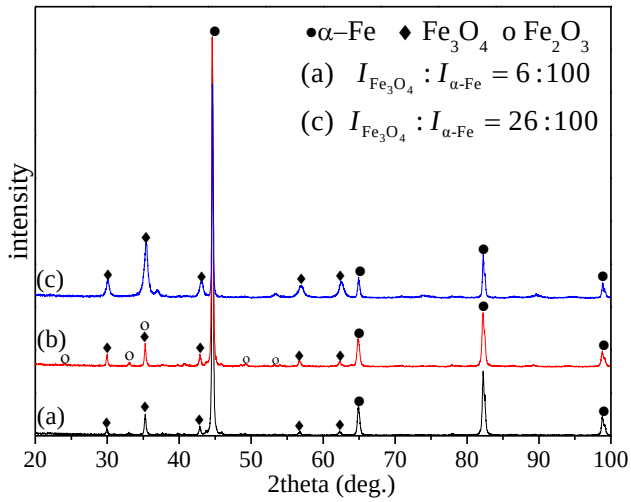

Fig. 3 XRD diffraction patterns of 45 steel samples treated by different peroxidation (a) APO 350℃×45 min; (b) APO 350℃×60 min; (c) SPO 350℃×45 min

DOI 10.12776/ams.v25i2.1271 p-ISSN 1335-1532
e-ISSN 1338-1156

3.4 Surface morphology

Fig. 4 shows the surface morphology of sample treated by different preoxidation process. It clearly shows that the structure of oxide layer treated by air preoxidation is lamella in shape. But the sample treated by salt bath preoxidation has a rough oxide layer with a lot of nano- pores. Obviously the sample treated by salt bath preoxidation has bigger specific surface area than that treated by air preoxidation, thus has larger contact area with the active nitrogen atoms in salt bath nitriding medium. Therefore, the oxide layer formed by salt bath preoxidation is easier to be reduced by active nitrogen atoms than that formed by air preoxidation. Meanwhile, nano-pores can help the active nitrogen atoms to diffuse into the substrate.

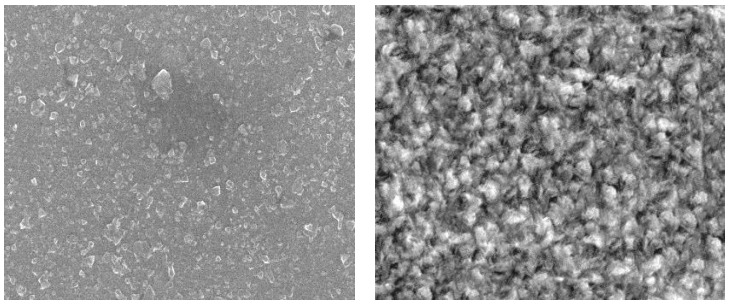

a b

Fig. 4 The surface morphology of sample treated by different preoxidation methods (a) APO 350℃×45 min; (b) SPO 350℃×45 min

4 Discussion

During preoxidation reaction, the chemical bonds of NO_3^- (comes from $NaNO_3$) in salt bath preoxidation medium and O^2 in air are discomposed to generate active oxygen atoms by absorbing energy, and the bonding energy of O-N and O=O is 206kJ/mol and 498kJ/mol, respectively, which illustrates that O-N in salt bath medium is much easier to decompose and form active oxygen atoms than that of O=O in air. Therefore, the reaction between Fe and molten $NaNO_3$ is much faster than that between Fe and O_2 at the same preoxidation temperature, leading to higher relative content of Fe_3O_4 by salt bath preoxidation (**Fig. 3**). In addition, when air preoxidation time increases to 60min, the Fe_2O_3 phase is formed on the sample surface. This indicated that too much holding time result in excessive oxidation to form Fe_2O_3 phase, which was unfavorable for subsequent nitriding [22, 23]. Therefore, the enhancement effect of air preoxidation cannot be consistently increased through extended holding time.

Fig. 4 shows that the sample treated by salt bath preoxidation has bigger specific surface area than that treated by air preoxidation, thus the oxide layer formed by salt bath preoxidation is easier to be reduced by active nitrogen atoms. Meanwhile, nano- pores can help the active nitrogen atoms to diffuse inward to the substrate.

5 Conclusions

The effect of salt bath preoxidation and air preoxidation on salt bath nitriding was compared, and The results showed that salt bath preoxidation has better enhancement effect on salt bath nitriding. The thickness of compound layer is only 13.3μm treated by air preoxidation, and increased to 20.8μm treated by salt bath preoxidation while nitrided at 560°C for 120min. Meanwhile, the sample treated by salt bath preoxidation has higher cross-section hardness than that treated by air

DOI 10.12776/ams.v25i2.1271 p-ISSN 1335-1532
e-ISSN 1338-1156

preoxidation. The enhancement mechanism is that the sample treated by salt bath preoxidation has higher relative content of Fe_3O_4, which can react with active nitrogen atoms in salt bath nitriding to accelerate the growth of Fe_3N.

References

[1] R. Bidulský, J. Bidulská, M. Actis Grande: Metal Science and Heat Treatment, Vol. 58, 2017, No. 11-12, p. 734-737, https://doi.org/10.1007/s11041-017-0087-z
[2] W. Cai, F. N. Meng, X. Y. Gao, J. Hu: Applied Surface Science, Vol. 261, 2012, p. 411-414, https://doi.org/10.1016/j.apsusc.2012.08.024
[3] Y. Z. Shen, K. H. Oh, D. N. Lee: Scripta Materialia, Vol. 53, 2005, No. 12, p. 1345-1349, https://doi.org/10.1016/j.scriptamat.2005.08.032
[4] H. T. Fu, J. Zhang, J. F. Huang, Y. Lian, C. Zhang: Journal of Materials Engineering and Performance, Vol. 25, 2016, No. 1, p. 3-8, https://doi.org/10.1007/s11665-015-1762-0
[5] Z. S. Zhou, J. Hu: Surface Engineering, Vol. 25, 2015, No.1, p. 613-615, https://doi.org/10.1179/1743294415Y.0000000076
[6] X. Y. Ye, J. Q. Wu, Y. L. Zhu, J. Hu: Vacuum, Vol. 110, 2014, p. 74-77, https://doi.org/10.1016/j.vacuum.2014.08.015
[7] J. Q. Wu, H. Liu, X. M. Ye, Y. T. Chai, J. Hu: Journal of Alloys and Compounds, Vol. 632, 2015, No. 5, p. 397-401, https://doi.org/10.1016/j.jallcom.2015.01.221
[8] R. Bidulský, M. Actis Grande, E. Dudrova, M. Kabatova, J. Bidulská,: Powder Metallurgy, Vol. 59, 2016, No. 2, p. 121-127, https://doi.org/10.1179/1743290115Y.0000000022
[9] Z. S. Zhou, M. Y. Dai, Z. Y. Shen, J. Hu: Journal of Alloys and Compounds, Vol. 623, 2015, p. 261-265, https://doi.org/10.1016/j.jallcom.2015.01.221
[10] J. C. Li, X. M. Yang, S. K. Wang, K. X Wei, J. Hu: Materials Letters, Vol. 116, 2014, p. 199-202, https://doi.org/10.1016/j.matlet.2013.11.033
[11] M. Y. Dai, Y. Chen, Y. T. Chai, et al.: Surface Review and Letters, Vol. 23, 2016, https://doi.org/10.1142/S0218625X16500499
[12] Z. S. Zhou, M. Y. Dai, Z. Y. Shen, J. Hu: Vacuum, Vol. 109, 2014, p. 144-147, https://doi.org/10.1016/j.vacuum.2014.07.016
[13] Y. Li, L. Wang, D. D. Zhang, et al.: Journal of Alloys and Compounds, Vol. 497, 2010, No. 1-2, p. 0-289, https://doi.org/10.1016/j.jallcom.2010.03.027
[14] D. Manfredi, R. Bidulský: Acta Metallurgica Slovaca, Vol. 23, 2017, No. 3, p. 276-282, https://doi.org/10.12776/ams.v23i3.988
[15] R. B. Huang, J. Wang, S. Zhong, M. X. Li, J. Xiong, H. G. Fan: Applied Surface Science, Vol. 271, 2013, p. 93–97, https://doi.org/10.1016/j.apsusc.2013.01.111
[16] J. Wang, Y. H. Li, J. Yan, D. Z. Zen, Q. Zhang, R. B. Huang, et al.: Surface & Coatings Technology, Vol. 206, 2012, No.15, p. 3399–3404, https://doi.org/10.1016/j.surfcoat.2012.01.063
[17] Y. S. Niu, R. H. Cui, Y. T. He, Z. M. Yu: Journal of Alloys and Compounds, Vol. 610, 2014, p. 294–300, https://doi.org/10.1016/j.jallcom.2014.04.193
[18] M. F. He, L. Liu, Y. T. Wu, C. Zhong, W. B. Hu, D. Pan: Journal of Alloys and Compounds, Vol. 551, 2013, p. 389–398, https://doi.org/10.1016/j.jallcom.2012.11.005
[19] G. J. Li, Q. Peng, C. Li, Y. Wang, J. Gao, S.Y. Chen, et al.: Materials Characterization, Vol. 59, 2008, No. 9, p. 1359–1363, https://doi.org/10.1016/j.matchar.2007.11.002
[20] Shih, T. Shih , Y. S. Huang , C. F. Chen: Applied Surface Science, Vol. 258, 2011, No. 1, p. 81-88, https://doi.org/10.1016/j.apsusc.2011.08.010

[21] G. J. Li, Q. Peng, J. Wang, C. Li, Y. Wang, J. Gao, et al.: Surface and Coatings Technology, Vol. 202, 2008, No. 13, p. 2865–2870, https://doi.org/10.1016/j.surfcoat.2007.10.032
[22] G. Y. Xiong, M. J. Zhao, L. Z. Zhao, et al., Advanced Materials Research, 2010, No. 97-101, p. 1454-1458, https://doi.org/10.4028/www.scientific.net/amr.97-101.1454
[23] P. Jacquet, J. B. Coudert, P. Lourdin: Surface & Coatings Technology, Vol. 205, 2011, No.16, p. 4064–4067, https://doi.org/10.1016/j.surfcoat.2011.02.049

Acknowledgements

The research was supported by National Natural Science Foundation of China (51774052), Top-notch Academic Programs Project of Jiangsu Higher Education Institutions (TAPP), Priority Academic Program Development of Jiangsu Higher Education Institutions (PAPD2018-6).